Article

The Hydrothermal Alteration of the Cordón de Inacaliri Volcanic Complex in the Framework of the Hidden Geothermal Systems within the Pabelloncito Graben (Northern Chile)

Santiago Nicolás Maza [1], Gilda Collo [2,3], Diego Morata [1,*], Carolina Cuña-Rodriguez [4], Marco Taussi [5] and Alberto Renzulli [5]

1 Department of Geology and Andean Geothermal Center of Excellence (CEGA), Facultad de Ciencias Fisicas y Matematicas, Universidad de Chile, Plaza Ercilla 803, Santiago 8370450, Chile; santiagomaz@gmail.com
2 Consejo Nacional de Investigaciones Científicas y Tecnológicas (CONICET), Centro de Investigaciones en Ciencias de la Tierra, Córdoba X5016GCA, Argentina; gildacollo@unc.edu.ar
3 Department of Geography, Facultad de Filosofía y Humanidades, Universidad Nacional de Córdoba, Córdoba X5016GCA, Argentina
4 Facultad de Ciencias Puras y Naturales, Carrera de Biología, Universidad Mayor de San Andrés, La Paz P.O. Box 10077, Bolivia; ccunarodriguez@gmail.com
5 Dipartimento di Science Pure e Applicate, Università degli Studi di Urbino Carlo Bo, Via Cà le Suore, 2/4, 61029 Urbino, Italy; marco.taussi@uniurb.it (M.T.); alberto.renzulli@uniurb.it (A.R.)
* Correspondence: dmorata@ing.uchile.cl

Abstract: Detailed mineralogical analyses in areas with surface hydrothermal alteration zones associated with recent volcanism (<1 Ma) in the Central Andean Volcanic Zone could provide key information to unravel the presence of hidden geothermal systems. In the Cordón de Inacaliri Volcanic Complex, a geothermal field with an estimated potential of ~1.08 MWe·km^{-2} has been recently discovered. In this work, we focus on the hydrothermal alteration zones and discharge products of this area, with the aim to reconstruct the geological processes responsible for the space-time evolution leading to the geothermal records. We identified (1) discharge products associated with acid fluids that could be related to: (i) acid-sulfate alteration with alunite + kaolinite + opal CT + anatase, indicating the presence of a steam-heated blanket with massive fine-grained silica (opal-CT), likely accumulated in mud pots where the intersection of the paleowater table with the surface occurred; (ii) argillic alteration with kaolinite + hematite + halloysite + smectite + I/S + illite in the surrounding of the acid-sulfate alteration; and (2) discharge products associated with neutral-alkaline fluids such as: (i) discontinuous pinnacle-like silica and silica deposits with laterally developed coarse stratification which, together with remaining microorganisms, emphasize a sinter deposit associated with alkaline/freshwater/brackish alkaline-chlorine water bodies and laterally associated with (ii) calcite + aragonite deriving from bicarbonate waters. The scarce presence of relics of sinter deposits, with high degree crystallinity phases and diatom remnants, in addition to alunite + kaolinite + opal CT + anatase assemblages, is consistent with a superimposition of a steam-heated environment to a previous sinter deposit. These characters are also a distinguishing feature of paleosurface deposits associated with the geothermal system of the Cordón de Inacaliri Volcanic Complex. The presence of diatoms in heated freshwater bodies at 5100 m a.s.l. in the Atacama Desert environment could be related with the last documented deglaciation in the area (~20–10 ka), an important factor in the recharge of the hidden geothermal systems of the Pabelloncito graben.

Keywords: clay minerals; surface hydrothermal alteration; steam heated; active geothermal system; diatoms; Cerro Pabellón; Andean Cordillera; Chile

1. Introduction

Active Andean volcanism (<1 Ma) makes the Chilean Andes a region with great potential in the development of geothermal energy, estimated, at least, in ~3000 MWe [1,2].

This intense volcanism leads to areas of superficial acid-sulfate alteration associated with a steam-heated blanket likely related to geothermal system [3–5]. Among the examples in central Chile, the active fumarole areas of Nevados de Chillan can be cited [6,7], which are linked to a hydrothermal-magmatic system, whereas in northern Chile these alteration zones have been identified in the acidic discharge sectors (upflow) of several areas, including the Cerro Pabellón hidden geothermal system [8–14].

The acid-sulfate stage is related to steam and gases (CO_2 and H_2S) that separate from deeper chloride-rich boiling fluids in vapor-dominated systems developed from hydrothermal-magmatic and/or geothermal sources, generating superficial steam-heated features such as fumaroles, mud pots and steaming ground, as well as the outflow of acidic water [3–5]. Distinctive surface and near-surface landforms and products such as steam-heated blankets, sinters, native sulfur deposits and altered rocks are associated with acid-sulfate stage.

A steam-heated blanket is formed from reactive H_2S-bearing fluids in the vadose zone above the groundwater table, and it can occur in the framework of high- (HS), intermediate- (IS) or low-sulfidation (LS) epithermal deposits [15–17] and/or geothermal fields [18,19]. This blanket is typically friable and consists primarily of fine-grained alunite, kaolinite and cristobalite, with different mineral associations mostly controlled by temperature (60–150 °C), pH and redox conditions [3–5], while the groundwater table, limiting the subhorizontal bases of the steam-heated zones, typically produces fine-grained porous to massive silicic rocks. Ancient steam-heated blankets generally have their friable upper parts eroded by weathering, only preserving the siliceous layers. The fluctuation of the groundwater table and various epithermal mineralization events can lead to multiple (and complex) levels of steam-heated blankets, e.g., Yanacocha, Peru, [20].

Identifying the type of deposits associated at depth with regions of development of steam-heated blankets can be a complex effort because these layers can mask diagnostic characteristics of the surface record of different epithermal environments. For example, the massive silicic rocks are diagnostic of acid lakes in high-sulfidation epithermal environments [3,21], and the sinters associated with intermediate- or low-sulfidation epithermal environments [3,16], can be confused with the very fine-grained silicic rocks of steam-heated environments, making identification difficult [22–25]. Establishing the genesis of silicic rocks and alteration mineral associations is critical in recognizing the different types of epithermal/geothermal deposits. In this context, investigations using Scanning Electron Microscopy (SEM) to observe mineral growth and transformation processes in siliceous rocks, which are related to physico-chemical parameters such as temperature, pressure, pH, redox state and time, may strongly help to address surface exploration [3,4,26,27].

This work is focused on the study of the hydrothermal mineralogy occurring in the Cordón de Inacaliri Volcanic Complex (CIVC), located in the Central Volcanic Zone of the Andes, near the Chile–Bolivia border. In the studied area, a significant 9 km^2 halo area of surface hydrothermal manifestations are identified [28]. In this paper, we will discuss the evolution of mineral parageneses of the hydrothermal alteration deposits of the CIVC, specifying the growth and transformation processes that occur in the silica phases, discriminating among steam-heated deposits, massive silica and sinters. This distinction will permit us to link the surface mineralogical records with the geothermal environments at depth and the potential primary control of the regional structures in the migration of hot fluids towards the surface.

2. Geological Overview

The CIVC is located between 4800 and 5200 m above sea level in the Antofagasta region (northern Chile), 45 km north of the El Tatio geysers and 9 km southeast from the Cerro Pabellón geothermal plant. The CIVC shares the same NW–SE tectono-morphological structure (the Pabelloncito graben) that controls the Cerro Pabellón geothermal field (Figure 1) [29]. A ~9 km^2 intense superficial, mainly fossil, hydrothermal alteration was observed in the volcanic deposits of the CIVC located inside the graben (Figure 1) and

includes local sites of steaming ground with soil temperatures ranging from 40 °C to 80 °C and diffuse CO_2 degassing, mainly related to an endogenous source [28].

The CIVC is part of the Pleistocene-age Palpana-Inacaliri volcanic chain [29–32] consisting of three main NW-SE-aligned stratovolcanoes, with the Inacaliri volcano itself located at the southern end of the graben [33] (Figure 1). The NW-SE graben orientation is coincident with the defined Andean Transversal Faults, which cross the Andean belt and constitute the main crustal routes for the migration of fluids towards surface [28,34]. Since 2017, the Cerro Pabellón geothermal field has been the only South American active geothermal power plant with a 48 MWe capacity already installed, with an additional 33 MWe that will be finally running by the end of 2021.
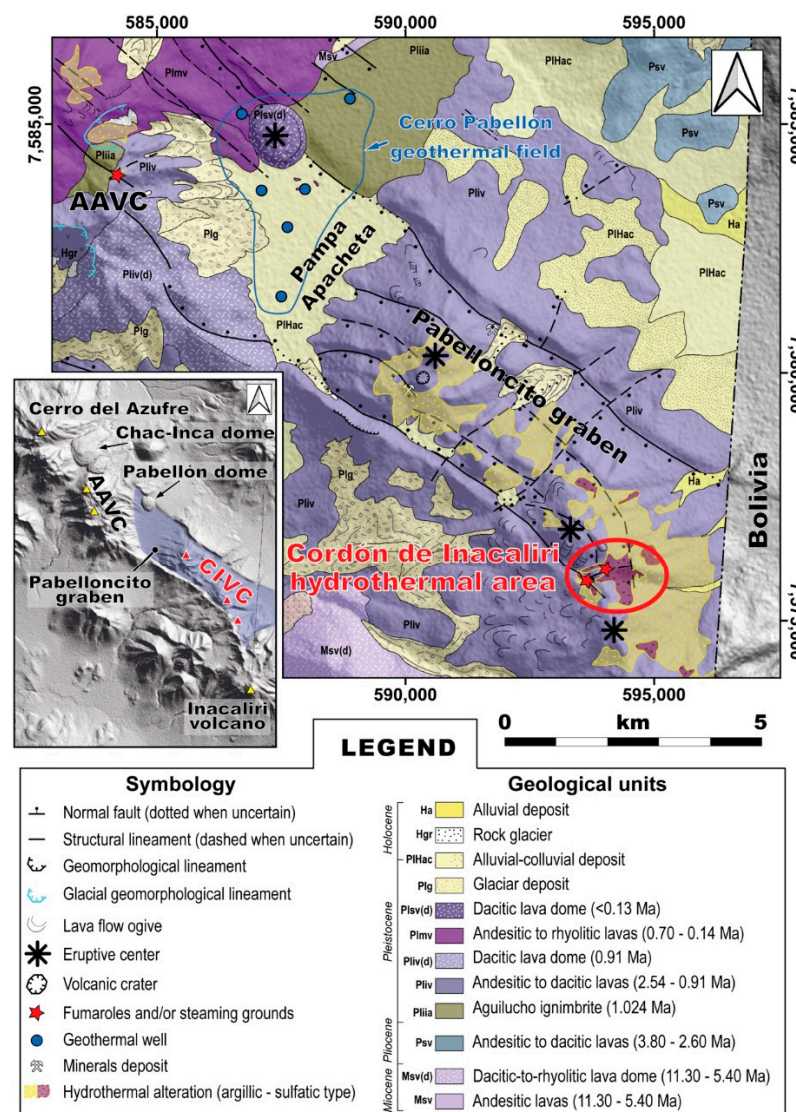
Figure 1. Simplified geological map of the Pabelloncito graben indicating the Cerro Pabellón geothermal power plant and the sampled areas of the Cordón de Inacaliri Volcanic Complex (CIVC) (modified from Taussi et al. [28] and Sellés and Gardeweg [31]).

3. Methodology

Thirty-six samples of hydrothermally altered rocks and silica deposits from the CIVC alteration zone were collected for this study. The sampling area was divided into 2 sectors and includes and widens the regions described by Taussi et al. [28]. The alteration zones developed parallel to the NW fault of the Pabelloncito graben in the western sector (CIWS), and parallel and transversely to this fault in the eastern sector (CIES), follow-

ing an ENE-striking lineament. In both sectors (CIES; samples IN-01 to 13; CIWS; samples IN-14 to 36), the sampling was carried out mainly in hydrothermally inactive and/or fossil areas. However, small crystals in concretions, altered rocks and silica deposits in specific active small zones (where heated soils were recorded), were also sampled. Some of these samples were subdivided into "a", "b", etc., specimens to distinguish sublevels of color or texture changes.

The mineralogical characterization of the collected samples was carried out using X-ray diffraction (XRD) on bulk rock and the clay fraction. The XRD data were obtained with a Bruker D8 Advance and D2 Phaser diffractometers, with Cu-Kα and Co-Kα radiation, respectively, and a Bragg-Brentano geometry at the Department of Physics in the Facultad de Ciencias Físicas y Matemáticas, Universidad de Chile. Samples for bulk rock analysis were dried at room temperature and 10 g were powdered in an agate mortar, examined through XRD between 2–80° 2θ and interpreted using the Match! 3.0 [35] software and quantified through the Reference Intensity Ratio (RIR) method [36].

The different phases of silica were identified by their characteristic reflections. The main diffraction bands for opal-A are centered at ~4 Å (~22.2° 2θCu-Kα; ~25.2° 2θCo-Kα), for opal-A/CT, opal-CT and opal-C at 4.09 Å (21.75° 2θCu-Kα; 24.75° 2θCo-Kα) and for quartz at 4.257 Å (20.85° 2θCu-Kα, 23.85° 2θCo-Kα) [25,37–43]. The degree of crystallinity of these phases was established from the ordering of the crystal lattice that is associated with the maximum width at the mean height (FWHM) of the different diffraction bands [44,45]. The order of the crystal lattice increases with growth and transformation, from non-crystalline opal-A and opal-A/CT to opal-CT and paracrystalline opal-C to, finally, microcrystalline quartz. FWHM values around 8.0° 2θ are characteristic of immature opal-A, whereas values around 0.2° 2θ are typical of microcrystalline quartz, cf. [25].

The mineralogy of the <2 μm fraction was studied in both active and fossil zones. Samples chips were: (i) washed in distilled water to remove salts, (ii) treated to remove organic matter and calcite, (iii) separated by centrifugation and iv) mounted in oriented aggregates [45]. XRD analyses of the clay fraction were carried out between 2 and 40° 2θ, with a step size of 0.02° 2θ and a scanning time of 1 s/step. The mineralogical identification of the clay fraction was conducted according to the positions of the basal reflections of air-dried (AD), ethylene-glycol solvated (EG), heated to 500 °C for 4 h (C) XRD patterns [45]. Semi-quantification was carried out through the Mineral Intensity Factor (MIF) method [45].

The textural and morphological changes of the silica phases during growth and transformation were analyzed in 10 samples from the alteration zone with a LEO VP1400 Field Emission Scanning Electron Microscope (FE-SEM) at the Laboratory of Experimental Physics of the Pontificia Universidad Católica de Chile. The samples were mounted on an aluminum stub and a SPI-MODULE sputter coater was used for Au–Pd alloy coating under operations conditions of 2 mbar, 15 mA, and 50 s. Operating conditions of FE-SEM were 15 keV accelerating voltage, spot size of 3 mm, and a working distance of 5 mm, 5–15 mA current, and 10–20 s counting time for each element.

After the characterization by XRD analyses, samples of the hydrothermal alteration zones containing kaolinites were selected for kaolinite crystallinity index (KCI) measurement [46]. Kaolinite was characterized in random powder samples (powder method) over a range of 15–40° 2θ in steps of 0.02° 2θ and a scan-step of 1 s. The 020, 110 and 11$\bar{1}$ reflections were used for Aparicio–Galán–Ferrell index (AGFI) calculations.

4. Results

4.1. Field Observations

In the CIVC hydrothermal alteration zone, an area of ≈9 km² of pervasively altered rocks was identified. In the CIWS, large inactive areas of whitish alteration, mostly composed by kaolinite-alunite (Figure 2A), isolated silica deposits (Figure 2B,C), some of them with pinnacle-like structures (Figure 2D), and fractures filled with carbonate deposits in the topographically higher areas (Figure 2E) were identified. Active zones are also associated with heated reddish and gray steaming grounds (40–80 °C, in situ measurements [28]),

surrounding the pinnacle-like structures, with few mineral precipitates in concretions and greenish to whitish centimetric efflorescence (Figure 2F).

Figure 2. Sampling sites (circled black points) in the alteration area of the Cordón de Inacaliri Western Sector (CIWS). (**A**) Steam-heated fossil alteration zone. (**B**,**C**) Relicts of silica deposits with a coarse stratification located at the periphery of the steam-heated area. (**D**) Pinnacle-like silica deposits located in the active zone. (**E**) Carbonate deposits filling vertical fractures in the periphery of the steam-heated area. (**F**) Concretions and efflorescence developed around or near pinnacle-like silica deposits in the active zone with diffuse gas emission, and a detail (inset) of the contact of the oxidized surface with the kaolinite-rich layer occurring few centimeters below.

In the CIES, the inactive zones are associated with an extensive development of the whitish kaolinite-alunite rich regions along and parallel to the NW-striking lineaments of the Pabelloncito graben (Figure 3A,B). These whitish areas are also recognized along the ENE-striking ridge (Figure 3A,C,D), where massive vertical fossil structures composed of sulfates also occur. At the intersection of these lineaments, local zones of steaming ground are also recognized (Figure 3B).
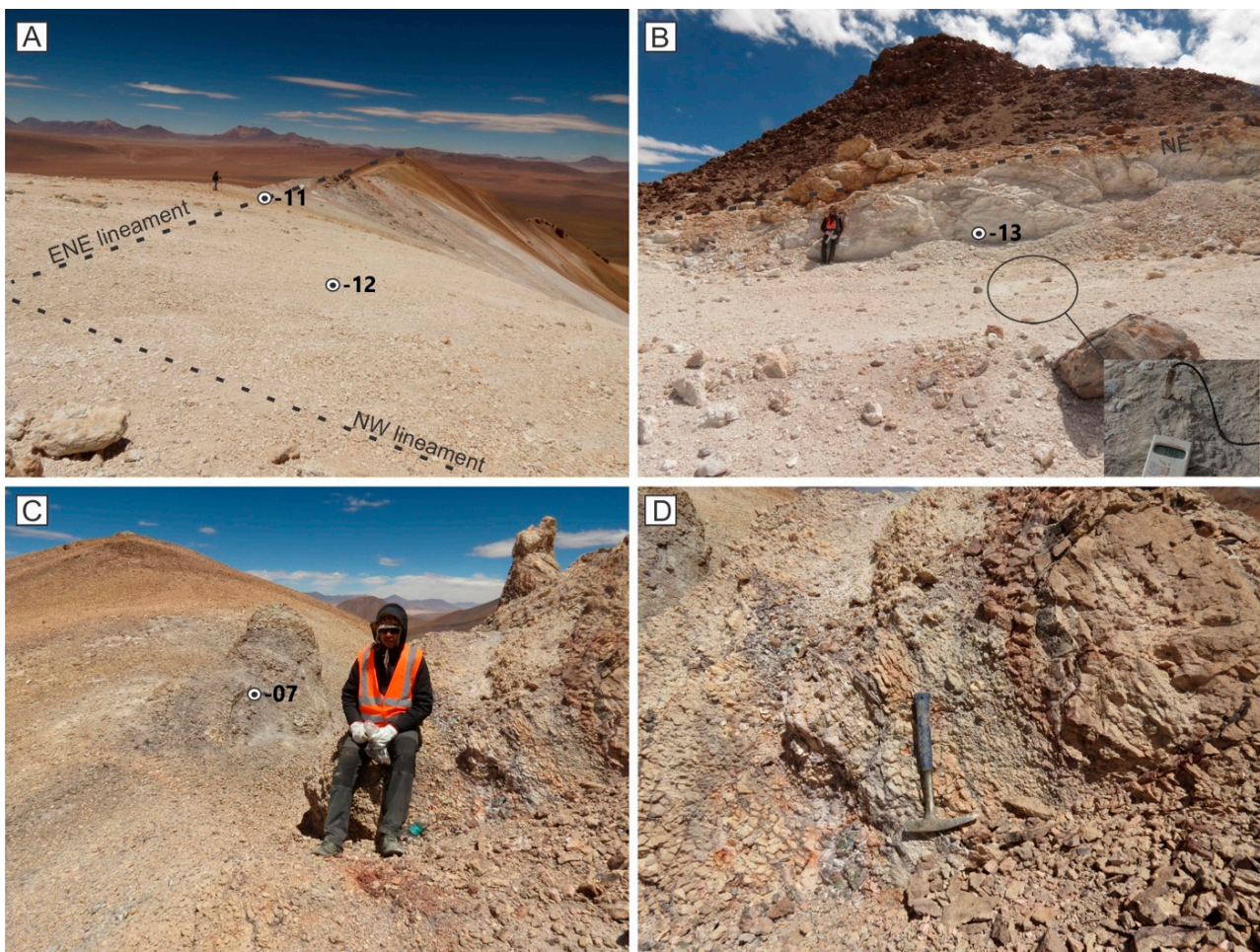
Figure 3. Sampling sites (circled black points) in the alteration area of the Cordón de Inacaliri Eastern Sector (CIES). (**A**) Steam-heated fossil alteration zone with dashed line showing the trace of the NW and ENE lineaments. (**B**) Sample at the intersection of the NW and ENE lineaments and the local zones of steaming ground (inset). (**C**) Massive vertical fossil structures composed mainly of sulfates. (**D**) Close up of the sample site 07 in (**C**).

4.2. Alteration Zone Mineralogy

From the bulk rock and clay fraction XRD analyses, five mineral domains were identified in the CIES and the CIWS alteration sectors: 1—kaolinite-alunite-opal CT; 2—alunite-gypsum; 3—calcite domain; 4—kaolinite-hematite-halloysite-illite-smectite and 5—silica phases (Figure 4).

The kaolinite-alunite-opal-CT domain (1) is the dominant association in both sectors (Figure 4). This mineral association is composed by kaolinite (~36%), alunite (~36%) and opal-CT (~28%), with anatase and (rare) opal-A (Figures 4 and 5) as minor components. Kaolinite, accompanied by traces of illite, shows the highest proportions (~80%) at the intersection of the NW and ENE lineaments and dominates the clay fraction. Analyses of the reflections located between 20–25° 2θ suggest a high index of crystallinity (~1.56, KCI) for kaolinites. The FE-SEM images highlight hexagonal crystals ~2 μm in size as book-like stacks of platelets (Figure 6A,B) which are consistent with the relative crystallinity values. In addition, a second population of individual hexagonal crystals of ~500 nm in size, with acicular halloysite and anatase crystals (Figure 6C), was also identified.
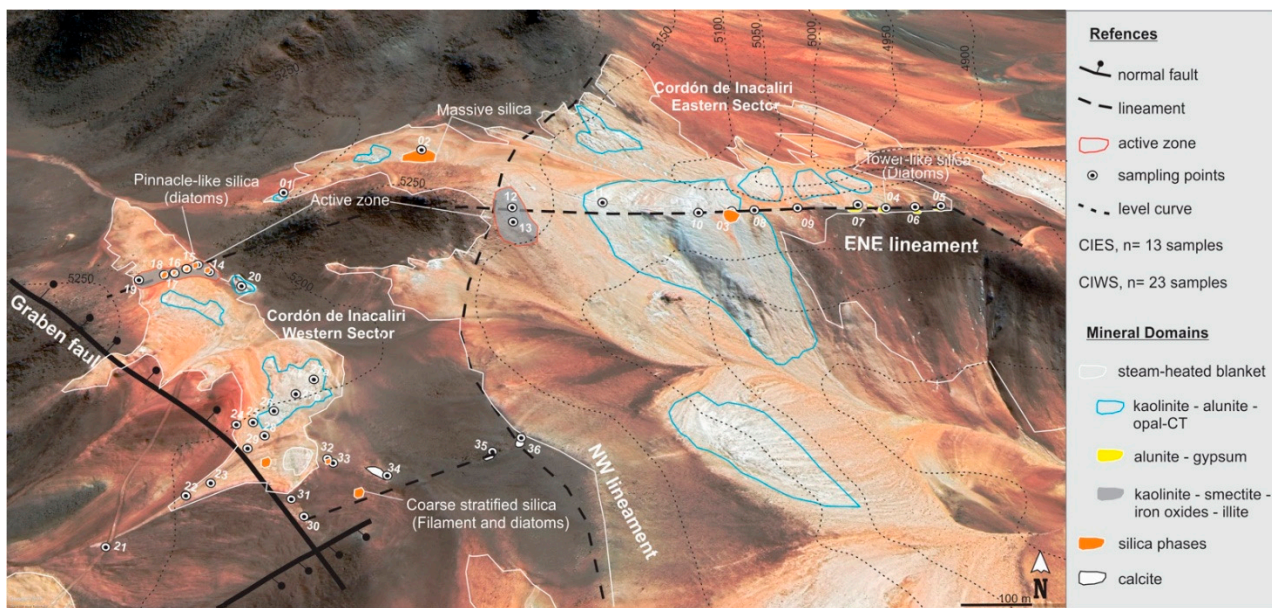
Figure 4. Satellite image of the study area. Steam-heated areas, sampling points, mineral domain zones and the Pabelloncito graben normal faults and lineaments cited in the text are indicated. Active zones occur with limited development and are indicated by a red contour. In the silica phases (5), the location of the different types of silica deposit and microorganism identified were also indicated.

The alunite-gypsum domain (2) was developed mainly in the CIES, at the end of the ENE lineament, and is represented by alunite (20–94%) and gypsum (4–83%) as the main phases (samples IN-04, 05, 06, 07, 08), associated with quartz, cristobalite and opal-A in variable proportions (Figures 4 and 5). Negligible amounts of kaolinite, even rarer mixed-layer R0-type I/S (~85% Sm), illite and, only in one sample, smectite were identified in this domain. Layered gypsum (Figure 6D) and alunite crystals with etched and pitted exterior surfaces (interpreted as the result of condensate acidic steam leaching) were also observed (Figure 6A).

The calcite domain (3) was only observed in the CIES in relation to vertical fractures of the volcanic rocks in the higher altitude areas, at the periphery of the kaolinite-alunite-opal-CT domain (Figures 2E, 4 and 5). Calcite (between 20–75%), together with tridymite (30–70%), cristobalite (<3%) ± aragonite, are the main identified phases. Noteworthily, an increase of the proportion of calcite with altitude, coupled with a decrease of tridymite, was observed.

The kaolinite-hematite—halloysite-illite-smectite domain (4) developed in the active zones of the CIES, on steaming grounds (Figures 2F, 4 and 5) superimposed or developed together with alunite-anatase (domain 1) and quartz (domain 5). This domain (4) consists of kaolinite (3–25%), hematite (5–45%), opal-CT (8–15%), illite (1–10%) and halloysite (1–5%). The <2 μm fraction also shows the presence of illite and smectite. Concretions and saline efflorescence formed by alunogen and cristobalite were also observed.

The silica phase domain (5) is only locally recognized, mainly in the CIWS and in some few points of the CIES. It consists of three different types of deposits, whose areal distribution varies from ~20 cm to 1 m: 1—massive silica deposits with lateral development as surface layers within the fossil zone (domain 1, Figures 4 and 5); 2—discontinuous pinnacle-like deposits (Figures 4 and 5) surrounded by red active steaming ground (domain 4); and 3—deposits with lateral development characterized by a coarse stratification (Figures 4 and 5), which occur, mainly, as relict and/or as boulders, associated with the periphery of the fossil zone (domain 1).
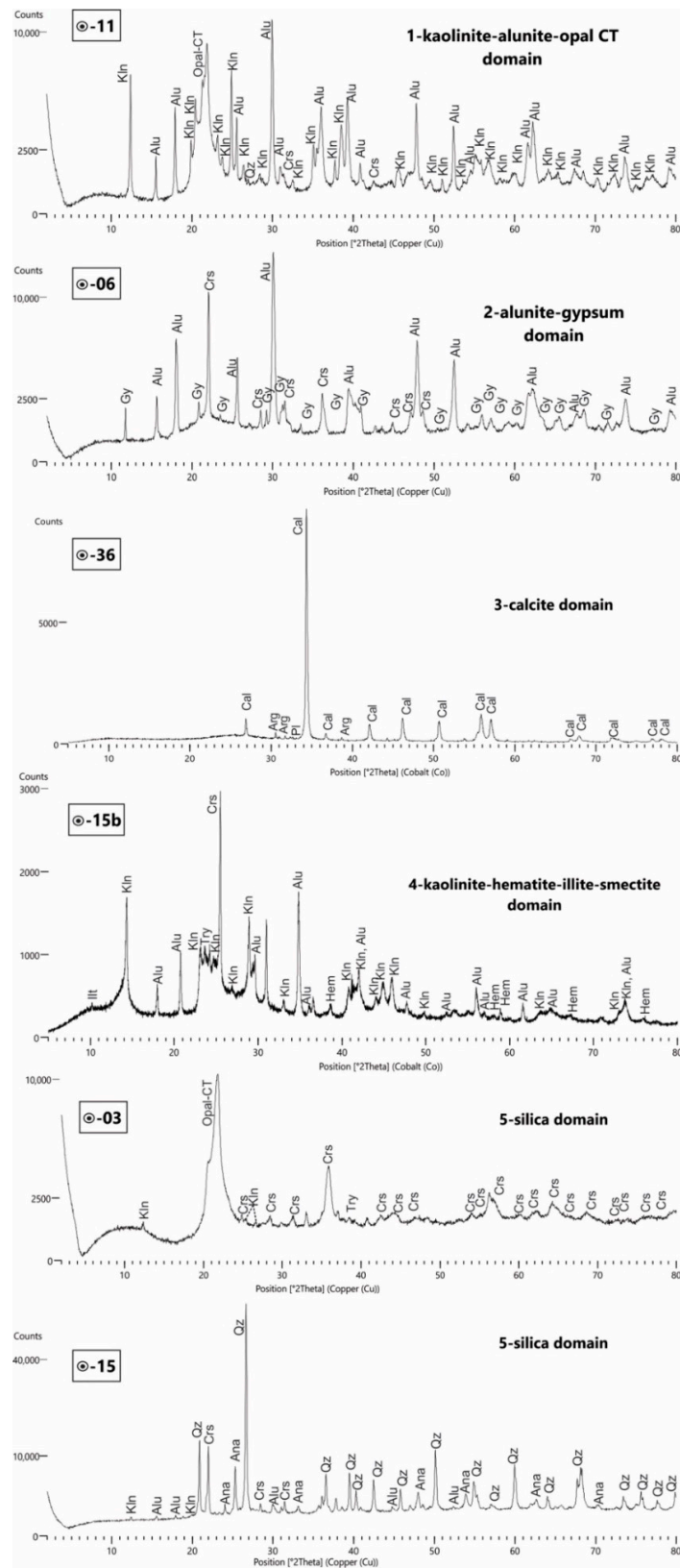
Figure 5. Representative X-ray powder diffraction patterns of the mineral domains in the hydrothermal alteration zone of the Cordón de Inacaliri Volcanic Complex. Abbreviations: alunite (Alu); anatase (Ana); aragonite (Arg); calcite (Cal); cristobalite (Crs); gypsum (Gp); hematite (Hm); illite (Ilt); kaolinite (Kln); opal-CT (opal-CT); plagioclase (Pl); quartz (Qz); tridymite (Try).
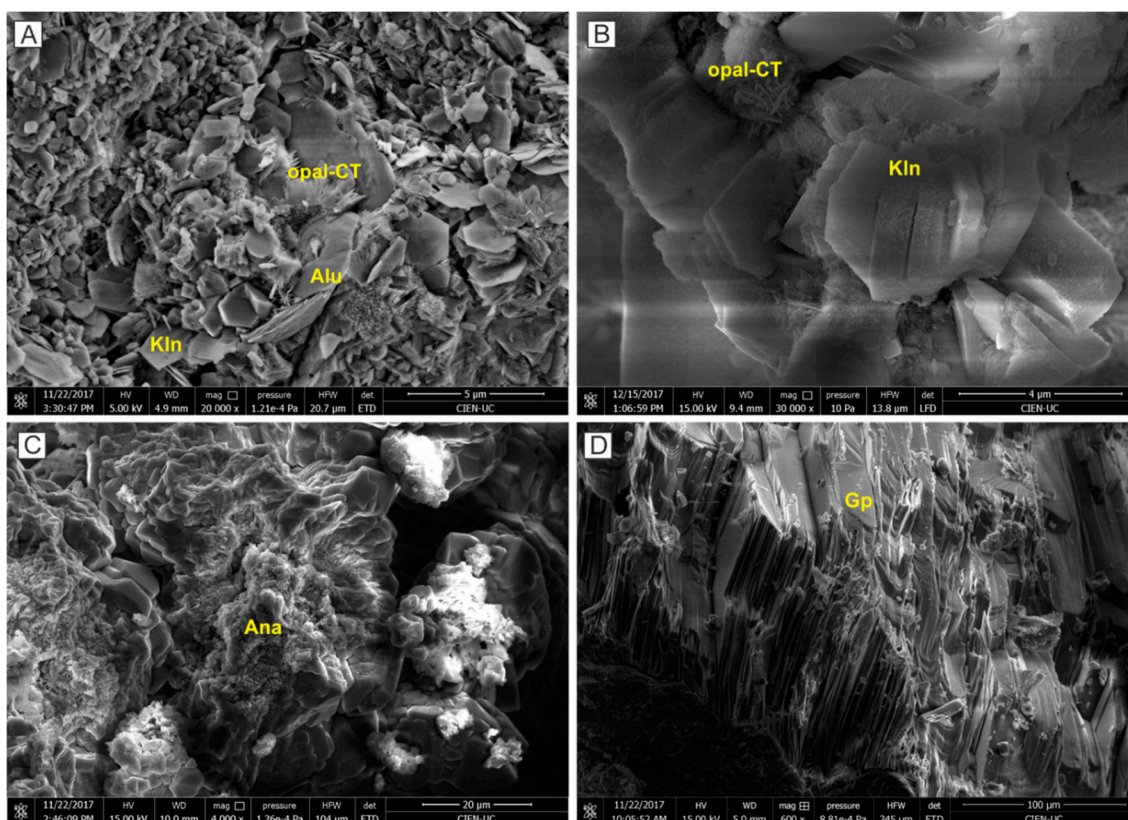
Figure 6. (**A**) SEM-images of the mineral domain (1) showing lepisphere crystals of opal CT, hexagonal crystals of alunite and kaolinite. (**B**) Detail of kaolinite with hexagonal crystals ~2 μm in size as book-like stacks of platelets. (**C**) Opal-C and microcrystals of quartz and anatase crystals as aggregates. (**D**) Layered gypsum crystals. Abbreviations: alunite (Alu); anatase (Ana); opal-CT; gypsum (Gp); kaolinite (Kln).

4.3. Description of the Silica Deposits and the Mineralogical Transformation Processes
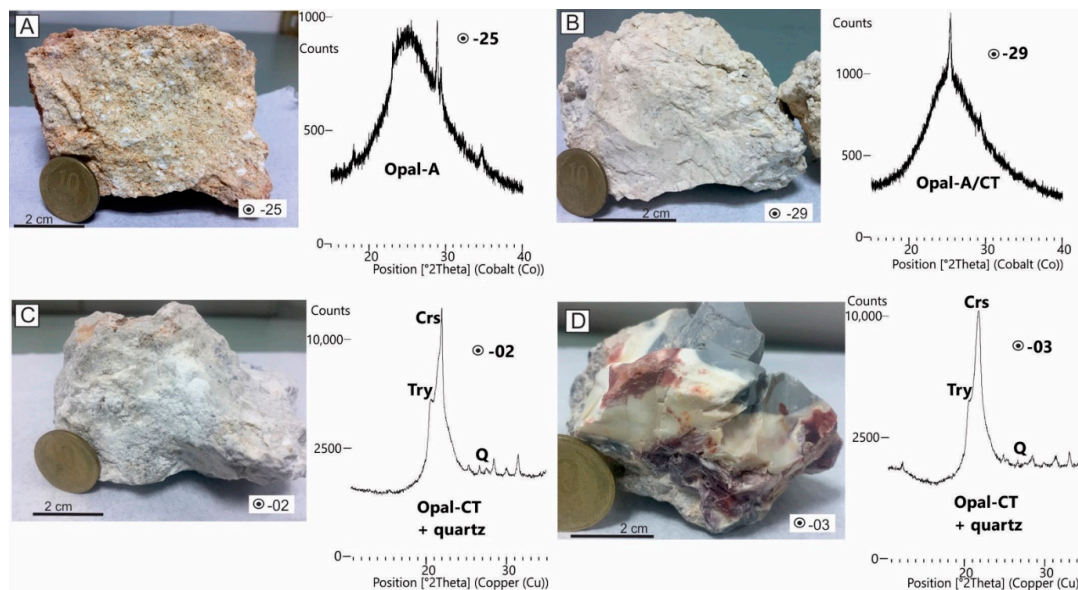
Massive silica deposits with lateral development as surface layers developed both in the CIWS and CIES. However, discontinuous pinnacle-like deposits and deposits with a coarse stratification were only observed in the CIWS.

4.3.1. Superficial Massive Silica Deposits with Lateral Development as Surface Layers

In these deposits, massive white (samples IN-02, Figures 2A, 4 and 7A) and banded silica textures (sample IN-03, Figure 7B) were recognized, consisting of cream-colored and brown silica in alternating centimetric levels. In the CIWS, these massive silica deposits have less areal distribution and mainly consist of discrete phases of opal-A (FWHM value of 7.7–5.8° 2θ) and opal-A/CT (FWHM value of 5.8–2.7° 2θ), while in the CIES, the deposits have greater lateral development and consist of opal-CT (FWHM value of 2.3–1.05° 2θ, Figure 6C,D) with lesser proportions of quartz. In both sectors, these silica deposits are associated with the kaolinite-alunite-opal-C domain (1). Quartz was also identified in sample IN-07 associated with the alunite-gypsum domain (2) and, only through FE-SEM analyses, in sample IN-13 associated with the kaolinite-alunite-opal-C domain (1).

Opal-A developed in a massive silica surface (sample IN-04, domain 2 alunite-gypsum) was identified as incipient semi-nanosphere particles and isolated nanospheres of ~120 nm in diameter, which are grouped in some sectors (Figure 8A,B). Furthermore, these particles also occur as botryoidal >9 μm size clusters cemented by smooth silica matrix (Figure 8C). On the other hand, micro-nanospheres (<1 μm) appear to be aligned in sets elongated into rows of <10 μm with a width of ~400 nm (Figure 8D; sample IN-07, domain 2: alunite-gypsum). The morphologies of grouped nanospheres and aligned micro-nanospheres have been described as part of the early and second step of silica phases corresponding to

the transformation from opal-A to opal A/CT [25,26]. This second step is marked by an increase in bumpiness on the smooth opal-A spheres.


Figure 7. Representative hand specimen photographs and XRD diagrams of the superficial massive silica deposits with lateral development as surface layers. (**A**) Porous and immature silica deposits consisting of opal-A with hematite patinas. (**B**) Massive white silica textures represented by opal-A/CT. (**C**) Massive white silica textures characterized by opal-CT with lesser proportions of quartz. (**D**) Banded silica textures with cream-colored and brown silica alternating and made of opal-CT with lesser quartz.
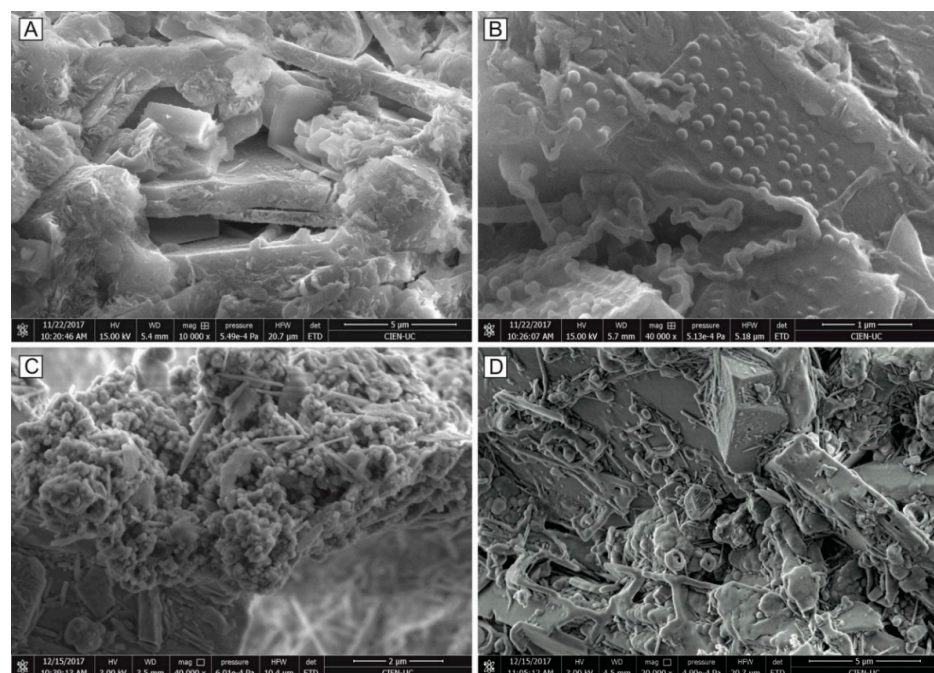
Figure 8. SEM-images showing morphologies of the first and second step of the transformation process from opal-A to microcrystalline quartz. (**A**) Semi-nanospheres of opal-A developed in a massive silica surface. (**B**) Detail of the nanospheres of opal-A. (**C**) Botryoidal clusters with a >9 μm extension of opal-A. (**D**) Morphologies of aligned micro-nanospheres corresponding to the second step of silica phases maturation.

When the aligned opal-A/CT nanospheres join to form beaded, somewhat jagged, plates, the development of classic opal-CT bladed lepispheres occurs (Figure 9A,B, sample IN-11, domain 1 kaolinite-alunite-cristobalite-anatase). These lepispheres retain an open structure consisting of very thin sheets or plates as spherical, randomly oriented aggregates of ~5 μm in diameter, which become parallel to each other when they are orthogonal to the silica surfaces (Figure 9C,D). These morphologies correspond to the third step of silica transformation process [25,26]. The randomly oriented bladed lepispheres occur after contact with individual hexagonal crystals of kaolinite, indicating that both are part of the same mineral assemblage (Figure 9E,F).
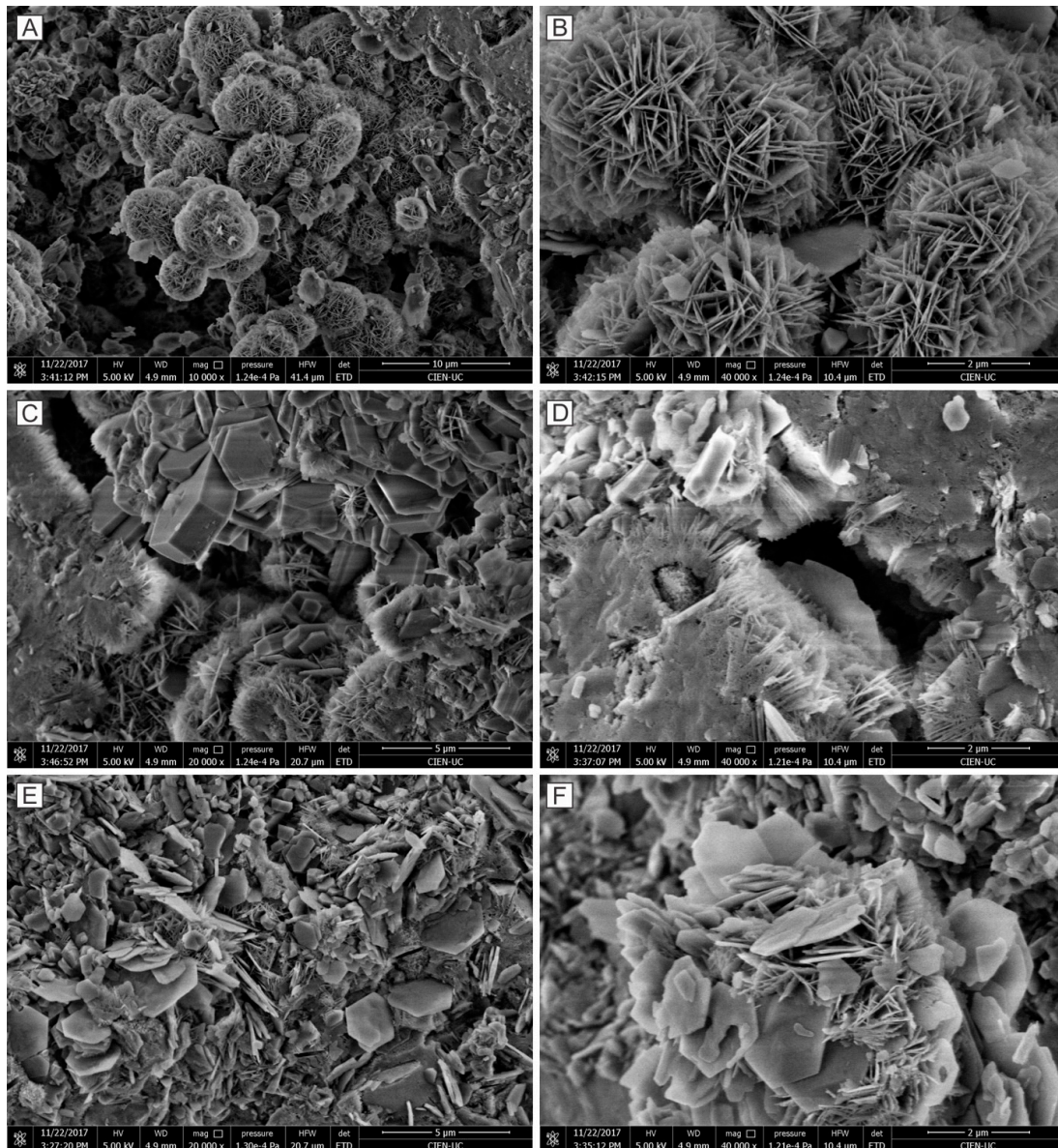
Figure 9. SEM-images showing morphologies of the third step of maturation from opal-A to microcrystalline quartz. (**A**) Mature opal-CT bladed lepispheres as spherical aggregates. (**B**) Detail of lepispheres showing open structures. (**C**) Lepispheres consisting of very thin sheets or plates randomly oriented or parallel to each other when they are orthogonal to the silica surfaces. (**D**) Detail of parallel sheets growing from massive silica. (**E**,**F**) Sheet or plates of opal-CT with hexagonal kaolinite crystals.

4.3.2. Discontinuous Pinnacle-like Silica Deposits

In these deposits, white-vitreous silica textures can be found alone (sample IN-17, Figures 2D, 4 and 10A) or coupled with angular and spatially irregular fragments (sample IN-20, Figure 10B). They are almost exclusively constituted by quartz (FWHM value of 0.15° 2θ) with lesser proportions of opal-C (FWHM value of 0.68–0.28° 2θ) and, in few sub-samples, opal-CT (Figure 9F).
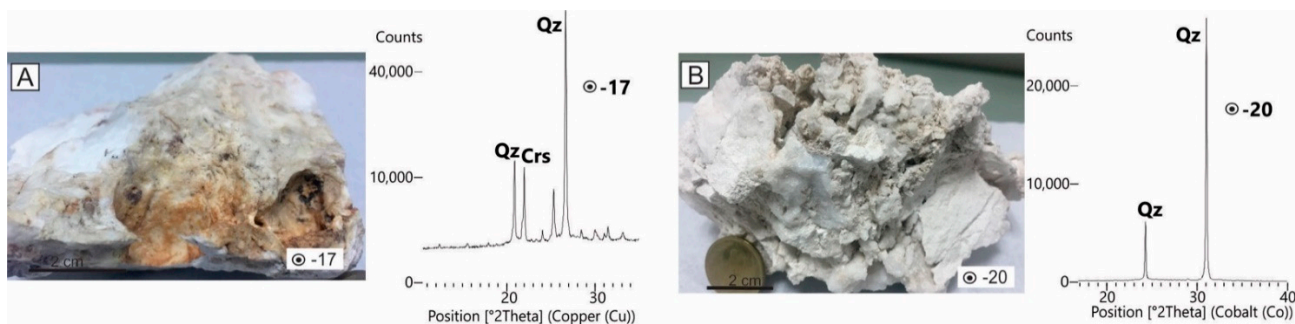
Figure 10. Representative hand specimen photographs and XRD diagrams of discontinuous pinnacle-like silica deposits. (**A**) White and vitreous silica texture preserving a semi-circular conduct constituted by quartz and cristobalite. (**B**) Spatially irregular fragments with white and vitreous silica textures of quartz.

In these samples, morphologies of blocky nanostructures of ~10 μm in diameter and clusters of nano-rods with a length of 15 μm were identified (Figure 11A–C; samples IN-14 and 15, domain 5 silica phases). Opal-C morphologies are also recognized in the domain 1 (kaolinite-alunite-opal-CT) associated with the intersection of the NW and ENE lineaments and locally affected by steaming grounds (sample IN-13), where thin to very thin randomly oriented plates were observed (sample IN-13, Figure 11D). These morphologies correspond to the fourth step of the transformation process [25,26] that leads to the change of opal-CT bladed lepispheres to randomly oriented thin to very thin plates or blocky nanostructures of opal-C.
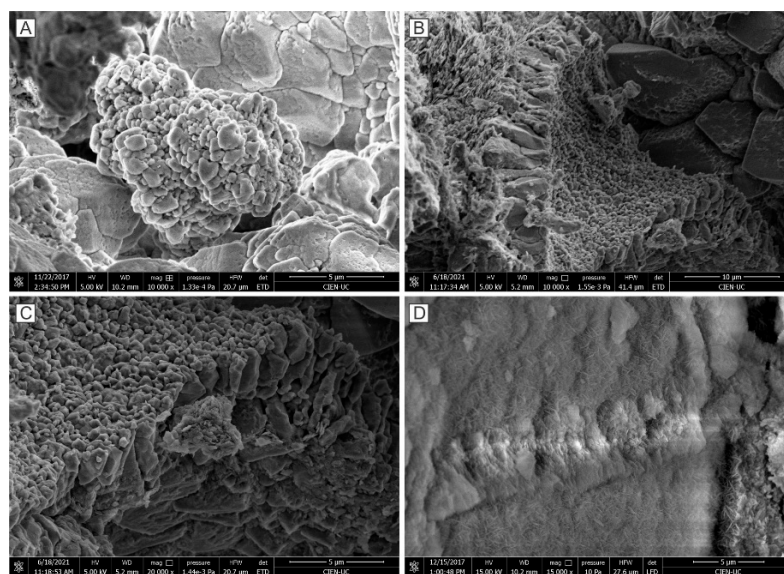
Figure 11. SEM-images showing the fourth-step transformation process from opal-A to microcrystalline quartz. (**A**) Opal-C morphologies of blocky nanostructures of ~10 μm in diameter. (**B**,**C**) Nano-rods of opal-C. (**D**) Thin to very thin randomly oriented plates of immature opal-C.

In these pinnacle-like silica deposits, the fifth step of the transformation process that leads to a restructuring of nano-rods or nanostructures of opal-C to microcrystalline quartz

was also observed. Hexagonal quartz crystals appear to be grouped with smooth and well-defined faces ~10 μm long (Figure 12A,B, sample IN-14 and 15, domain 5 silica phases). In some sectors, there are etched and pitted exterior surfaces related to acidic condensed steam attack (Figure 12C). Hexagonal quartz crystals were also identified, as well as opal-C morphologies, in the NW and ENE lineaments intersection zone (sample IN-13, domain 1), characterized by an individual development with smooth and well-defined faces with a length of 3–9 μm (Figure 12D,E).
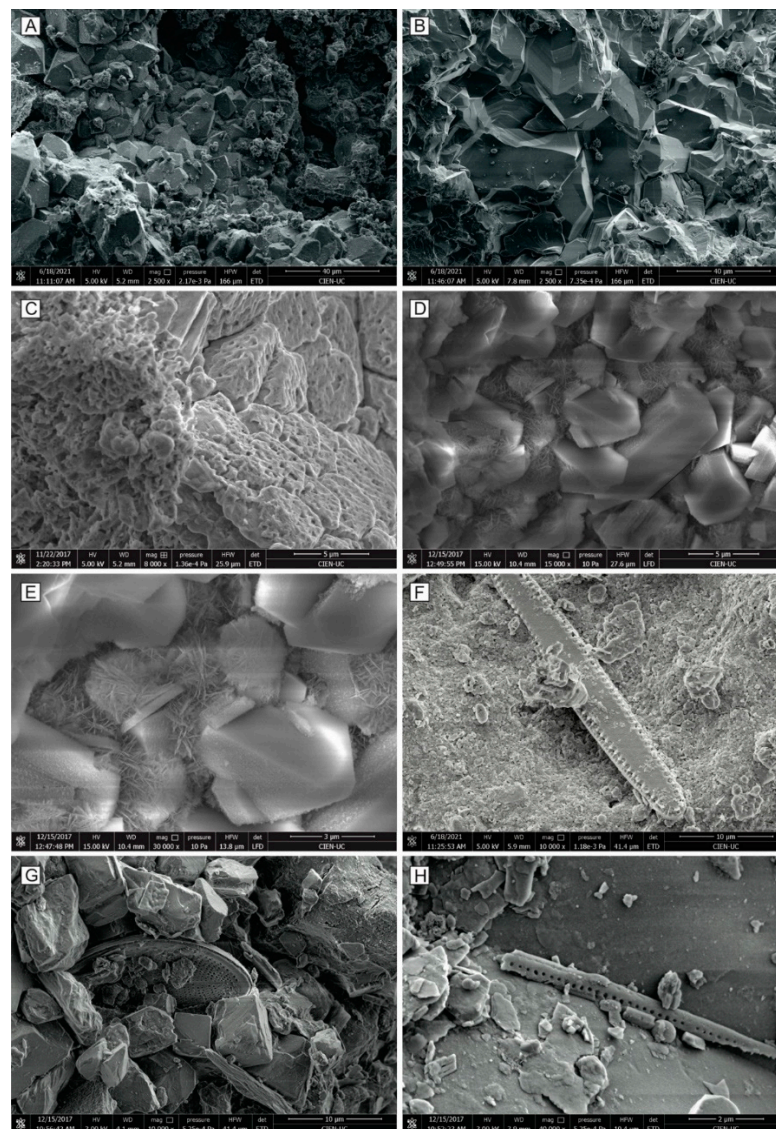
Figure 12. SEM-images showing the fifth step of the transformation process from opal-A to microcrystalline quartz and microorganism preserved. (**A**) Doubly terminated quartz microcrystals. (**B**) Clusters and bands of nanostructures at base, in stepped microcrystals of opal-C + quartz. (**C**) Etched and pitted exterior surfaces related to acidic condensed steam attack. (**D,E**) Hexagonal quartz crystals with an individual development with smooth and well-defined faces, and also lepispheres of opal-CT and nano-rods of opal-C. (**F**) Remnants of diatoms *Thalassionema nitzschioides (Grunow) Mereschkowsky*. (**G**) Remnants of diatoms *Cocconeis Placentula Ehrenberg* preserved in pinnacle-like sulfate deposit in the ENE-striking ridge area. (**H**) Fragments of diatoms valves and raphidean canals.

In these pinnacle-like silica deposits and in the ENE-striking ridge area, where pinnacle-like sulfate deposits were found, the presence of quartz was recognized, and remnants

of diatoms *Cocconeis Placentula Ehrenberg* and *Thalassionema nitzschioides (Grunow) Mereschkowsky* were found to be preserved (Figure 12F,G). These diatoms maintained the internal structures showing silicified valves and remnant from part of the raphidean canal (Figure 12H).

4.3.3. Silica Deposits with Laterally Developed Coarse Stratification

These silica deposits occur toward the peripheral zone affected by steam-heated alteration. They consist of an alternation of opaque white silica with porous reddish silica textures (sample IN-30, Figures 2B, 4 and 13A), and coarse laminated silica textures (sample IN-33) with an alternation of white and glassy levels and botryoidal textures surfaces (Figure 13B).
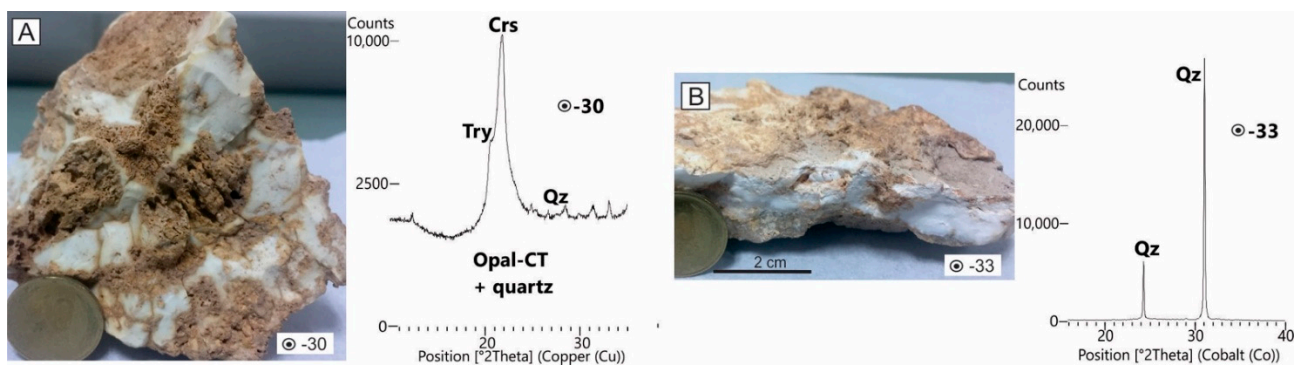
Figure 13. Representative hand specimen photographs and XRD diagrams of the silica deposits with laterally developed coarse stratification. (**A**) Alternation of opaque white silica and reddish porous silica with opaque white silica textures consisting of opal-CT and lesser amount of quartz. (**B**) Coarse laminated white and glassy silica textures of quartz.

Deposits with porous textures were identified as opal-CT (sample IN-30; FWHM value of 2.3–1.05° 2θ), while in laminated levels, quartz (sample IN-33; FWHM value of 0.15° 2θ) was recognized. These deposits show morphologies similar to those previously described, with hexagonal quartz grouped crystals (Figure 14A,B), and a lesser proportion of etched and pitted exterior surfaces associated with acidic condensed steams leaching. The preserved microorganisms are also similar, with remnants of diatoms *Amphora* sp. (sample IN-30; Figure 14C), remnants of diatoms from parts of valves and raphidean canal (Figure 14D), as well as fine to very fine filament textures of ~1.4–2.4 μm exterior diameters partially infilled or replaced by opal-A/CT (sample IN-33; Figure 14E,F). According to their diameters, these filaments are inferred to represent high temperature microbes [40].

The XRD results in the silica phases allowed us to identify more intense dissolution/precipitation and transformation processes in the CIWS (opal-CT, opal-C, quartz) than in the CIES (opal-A, opal-A/CT, opal-C). However, in the analyzed deposits, variations wereobserved in both the reflections and the FWHM values of the silica phases between samples with short vertical distances (<5 mm), thus indicating that the transformation processes between phases took place discontinuously.
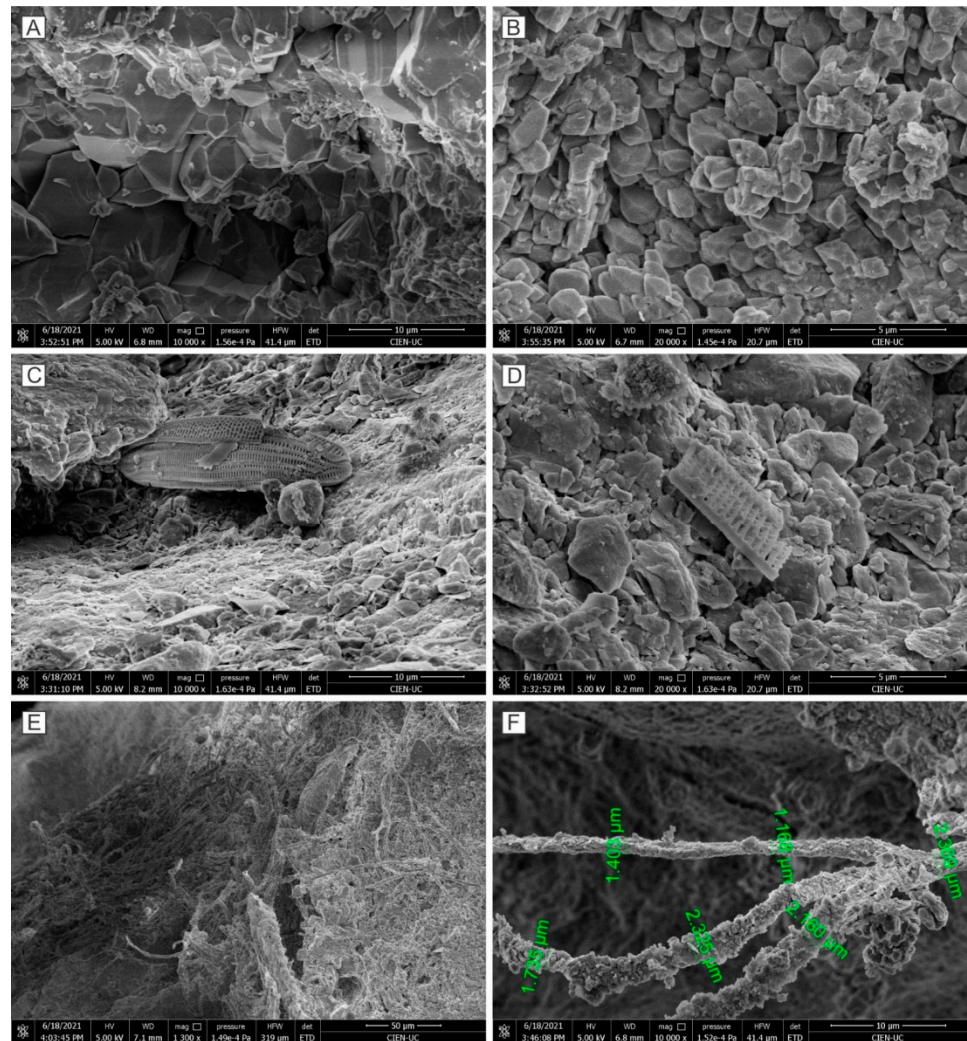
Figure 14. SEM-images showing the fifth step of the transformation process from opal-A to microcrystalline quartz and preserved microorganisms. (**A**) Well-developed quartz crystals with opal-C nanostructures. (**B**) Minor-developed quartz crystals with respect to those in Figure (**A**). (**C**) Remnants of diatoms *Amphora* sp. preserved in silica deposits with laterally developed coarse stratification. (**D**) Fragment of diatoms from part of valves and raphidean canals. (**E**) Silicified fine microbial filaments forming very porous filamentous networks. (**F**) Exterior diameter measurements of filaments partially infilled or replaced by opal-A/CT.

5. Discussion

5.1. Types of Alteration and Formation Environment

The different five mineralogical domains defined in the hydrothermally altered studied area, as well as the morphological and textural identified features, allow the definition of the following mineral assemblages:

(i).   kaolinite + alunite + opal-CT + anatase (domain 1);
(ii).   alunite + gypsum (domain 2);
(iii). calcite + aragonite (domain 3);
(iv).   kaolinite + hematite + halloysite + smectite + I/S + illite (domain 4);
(v).   opal-CT (domain 5);
(vi).   quartz (domain 5).

These mineral assemblages occur spatially superimposed and permit the definition of an acid-sulfate stage coexisting with neutral-alkaline and acid fluids surface and paleosurface discharge products, likely associated with the development of a geothermal

system. In order to outline a superficial dynamic space-time reconstruction of this complex environment of crystallization of the above assemblages, a series of discharge products are described below.

5.1.1. Discharge Products Associated with Acid Fluids

Acid-Sulfate Alteration

This alteration stage is represented by the mineral assemblages (i), (ii) and (v) (domains 1, 2 and 5). The assemblage (i) kaolinite + alunite + opal-CT + anatase shows the most widespread areal distribution (domain 1), and it is laterally associated with the assemblage (ii) alunite + gypsum and (v) opal-CT (see Figure 4). These mineral assemblages were identified both in the CIWS and the CIES, although the assemblage (ii) was mainly mapped in the CIES and discontinuously in the CIWS. The assemblage (v) opal-CT corresponds to superficial massive silica horizontal levels with discontinuous lateral development.

The assemblages (i), (ii) and (v) have been documented as part of the steam-heated blanket [3–5,12] and correspond to a zoned distribution within the upper and friable zone. The steam-heated blankets are formed in the vadose zone above groundwater table from acidic-pH fluids (pH < 4) produced by the condensation of vapors from geothermal waters with temperatures between 60–120 °C, which caused acid-sulfate alteration and consequently low density [3–5,15,47,48]. Much of the silica precipitated in the groundwater table typically derives from the dissolution of volcanic glass contained in tuffs, and forms in the vadose zone by condensed steams. The assemblage (v), precipitated at pH of ~2–3, could be the product of intense alteration from this acidic fluid, and it likely accumulated in mud pots where the intersection of the paleowater table with the surface may have occurred. Finally, assemblage (i) represents the typical spreading mineral association with acidic (pH 2–4) conditions [3–5]. The presence of alunite and gypsum in the assemblage (ii) could also be recorded in fumarole products of sulfates-bearing fluids, common in these systems, e.g., [47–52].

The acid-sulfate alteration was identified both in the active and fossil zones, and its elongated shape along the NW lineament is consistent with a structural control. In addition, it is also recorded along the ENE-striking ridge, where assemblages (i), (ii) and (v) corroborate the development of these steam-heated blankets. It is worth mentioning that at the intersection between both NW- and ENE-striking lineaments, there are areas of active steaming ground (>50 °C [28]) and elevated CO_2 emissions. Higher proportions of kaolinite with high crystallinity in these specific areas are consistent with higher temperature and/or permeability in superficial conditions [52,53].

Argillic Alteration

This alteration is defined by the assemblage (iv) kaolinite + hematite + halloysite + smectite + I/S (~85%Sm) + illite [4,16–18] and is documented in the CIWS along the ENE transversal lineament and as traces in the alunite + gypsum domain (domain 2), while developing in the active zones of the CIES on steaming grounds associated with quartz deposits (domain 5) or kaolinite + alunite + opal-CT + anatase (domain 1).

Assemblage (iv) appears to be associated with a steam-heated blanket and can be interpreted as a distal product of the same environment, reflecting the conditions of neutralization and cooling of acidic hydrothermal fluids likely produced by the interaction of the latter with the host rock and circumneutral meteoric waters, and/or with shallow aquifers [12,54–58]. In the same way, mixed-layer I/S + illite suggests slightly acidic to neutral conditions, although with higher temperatures than those inferred for smectite-kaolinite-halloysite association (i.e., 100–250 °C) [11,59–61], and a predominance of CO_2 vapors leading to the development of an argillic alteration below the superficial hydrothermal environment (and likely below the water table level) [16].

5.1.2. Discharge Products Associated with Neutral-Alkaline Fluids

These deposits are constituted by the assemblage (iii) and (vi) [3,4,62,63]. The assemblages (vi) quartz and (iii) calcite + aragonite were mapped in the CIWS towards the periphery of the zones affected by acid-sulfate alteration and as filling of vertical fractures. The assemblage (vi), composed by microcrystalline quartz, is associated with discontinuous pinnacle-like and other silica deposits with laterally developed coarse stratification.

The presence of biogenic material associated with microcrystalline quartz (diatoms and microbial filaments, see Section 4.3; Figures 12 and 14 for more detail) is consistent with alkali-chloride spring discharge [40,44], which would have taken place locally in the alteration areas of the CIVC. In this context, silica deposits can be interpreted as siliceous sinter generated from alkali-chloride hot spring discharge, derived from deep reservoirs with temperatures >175 °C [3,44,64]. The association of siliceous material with sinter deposits is also supported by the morphology of well-developed hexagonal microcrystal of quartz, diagnostic of dissolution/growth and transformation processes [26,65] linked to aging of the opal–quartz series, that allows to differentiate them from hydrothermal quartz deposits [25].

In the case studied here, silica deposits <1 m thick suggest a low flow rate during their formation. As these sinter deposits accumulate, distinctive textures were formed: (a) discontinuous pinnacle-like silica deposits related to high temperatures vents, and (b) silica deposits with laterally developed coarse stratification associated with intermedium and low temperatures in the distal areas. In the latter, filamentous textures associated with high temperatures in environments from intermediate to distal zones from the vent [40,41,65] were identified.

The presence of biogenic material in the sinters could be associated with the initial event of their formation, with a water temperature <100 °C [44], which allows the preservation of the biogenic (such as microbes or plants) and non-biogenic material present on the surface, thus recording paleoenvironmental conditions [65]. In this initial event, silica is deposited as non-crystalline opal-A. The coexistence of biogenic material and quartz makes it possible to interpret, on one hand, the environment of formation and, on the other hand, the superficial intense dissolution/growth and transformation processes of the initial opal-A to microcrystalline quartz.

Finally, calcite associated with these silica deposits, mainly filling fractures in slight to intermediate altered volcanic rocks, is interpreted as deriving from bicarbonate waters discharge product [3] in the most peripheral zones of the hot springs. Overall, the assemblages (vi) quartz and (iii) calcite are thought to be associated with a high-relief geothermal system [3].

5.2. Silica Deposits and Their Implications in the Reconstruction of the Subsurface Environment

As mentioned above, the study of surface and paleosurface products and their space-time relations could be very useful to discriminate their association with HS, IS or LS epithermal deposits at depth [3–5,15] and/or with geothermal systems. In the case of silica deposits, proximal sinters could suggest hidden IS to LS epithermal deposits, as well as the presence of geothermal reservoirs [18,19]. Instead, products associated with a steam-heated blanket, such as the groundwater table silicified and the friable surface layer, are less diagnostic features because they can alternatively occur above HS, IS or LS epithermal systems and, moreover, because they can be easily mistaken with silica deposits from other origin. Since geothermal systems can remain active even after the cessation of surface discharges, such as hot springs or fumaroles, ancient sinter deposits are an excellent tool in exploring blind or hidden geothermal fields [3,4,27].

The different mineralogical silica phases, linked to different mineral assemblages, in the alteration deposits of the CIVC, allow us to clearly discriminate two different compositional discharge records from silica deposits during the hydrothermal history (Figure 15). The first event (Figure 15B), characterized by sinter deposits, is typically formed from alkali-chloride hot spring discharges. The formations associated with this event are: (a) discontinuous pinnacle-like silica deposits and (b) silica deposits with laterally developed coarse stratification. Key and diagnostic features in these deposits include the

presence of biogenic materials associated with quartz recording the chemical composition of the fluids discharge at the surface, and the morphologies of hexagonal quartz crystals that indicate dissolution/growth and transformation processes [25,44].
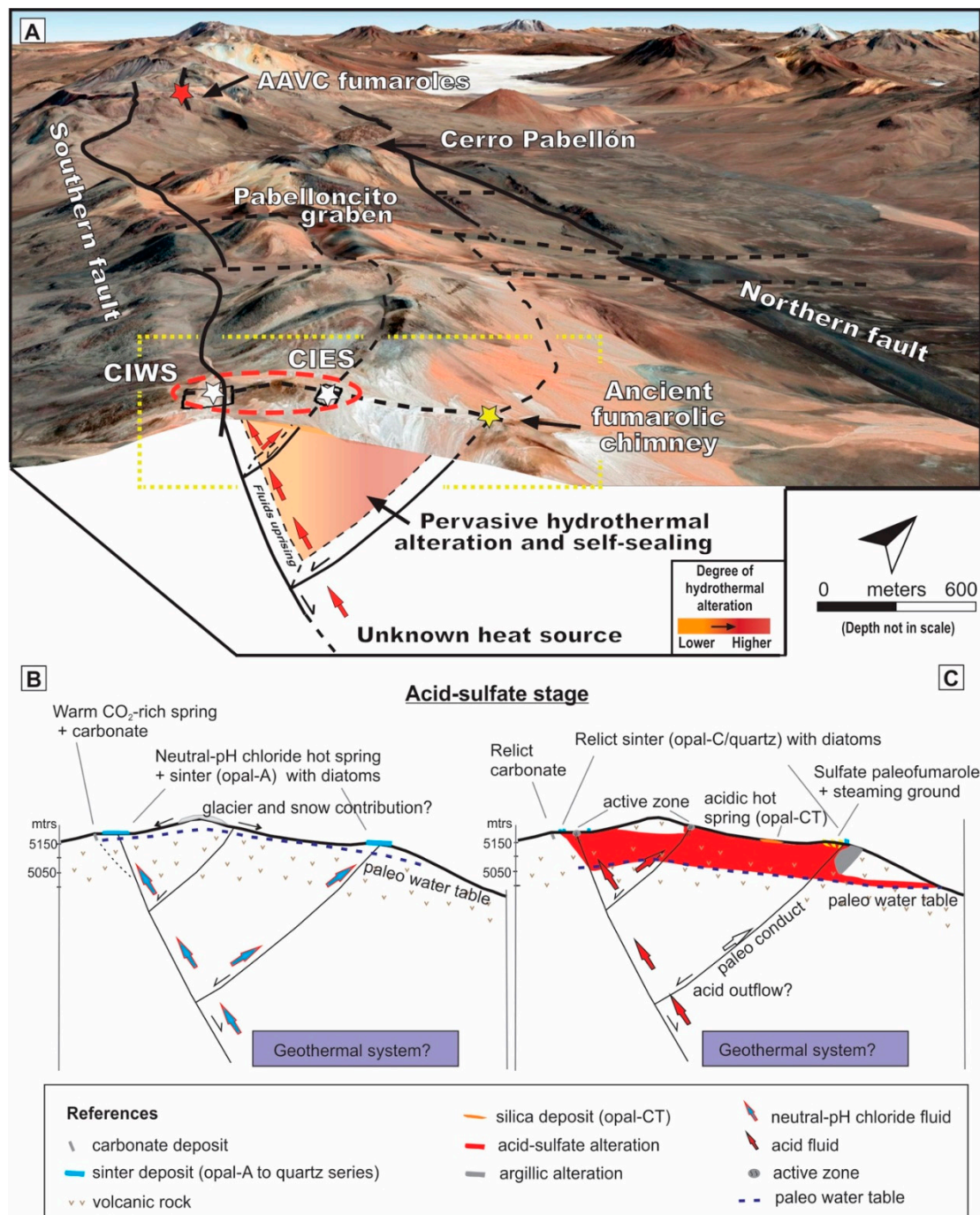
Figure 15. (**A**) Satellite image where the Pabelloncito graben, with the location of the Cerro Pabellón Geothermal System and the study area (yellow box in dotted lines) are shown. Furthermore, a structural scheme showing the control on the fluid migration towards the surface is presented (modified from Taussi et al. [28]). (**B**,**C**) Conceptual model showing the evolution of the acid-sulfate stage likely associated with a geothermal system at depth. The paleowater table position is shown. (**B**) Initial discharge of products related with the circulation of neutral waters (sinters with diatoms, carbonates); the likely glacier and snow contribution in the subsurface meteoric waters circulation is also pointed out. (**C**) Superimposed discharge products related to the circulation of acid-sulfate waters (steam-heated blankets), with a decline of the paleo-water table and an acid fluids outflow.

Both the *Thalassionema nitzschioides (Grunow) Mereschkowsky* and *Cocconeis Placentula Ehrenberg Amphora* sp. diatoms (Figures 12F,G and 14C), corresponding to benthic species that grows adhered to some substrate, identified in the CIWS sinters, as remnants filaments replaced by opal A/CT (Figure 14C,D), are characteristic of chlorine/saltwater and alkaline/freshwater/brackish environments, respectively. Diatoms have also been recognized in other alkaline geothermal environments associated with sinters such as those at the Steamboat Springs [44,64,66,67] and in recent deposits of the Atacama Desert [68]. The filaments appear to be laterally associated with calcite, which is consistent with the inferred alkali chloride waters discharge conditions for the formation of the biological material [40,65].

The second event (Figure 15C), characterized by deposits associated with steam-heated blanket, is closely linked to the formation of (1) massive fine-grained cream-colored silica (mainly opal-CT), with the typical morphology of bladed lepispheres and scarce or absent kaolinite-alunite and (2) the spread opal-CT linked to the kaolinite-alunite-opal-CT-anatase assemblage, which appears in friable to occasionally massive deposits. The former represents an acid discharge product where amorphous silica sediment accumulated in mud pots at the intersection of the paleo water table with the surface, or, alternatively, as an intense alteration product, while the latter is interpreted as the upper part of the steam-heated blanket. The biogenic material also appears in the CIES together with the alunite-gypsum domain associated with the steam-heated blanket, whose precipitation conditions (pH 2–4) are not consistent with the inferred alkaline discharge fluid. This constitutes a clear record of superimposition of an acidic discharge fluid (steam-heated blanket) and an alkaline discharge fluid (sinters).

In the area of an active steam-heated blanket with diffuse CO_2 degassing described by Taussi et al. [28] for the CIWS, quartz in the discontinuous pinnacle-like silica deposits surrounded by red soils with kaolinite-hematite-halloysite-smectite-illite (domain 4) coexists with gray soils with steam-heated alterations characterized by kaolinite-alunite-opal-CT-anatase and lesser proportions of alunogen (Figure 2F). The timing of these two contrasting compositional discharge in the study area can be inferred from the dissolution/growth and transformation processes identified in the silica phases from each deposit.

The microcrystalline quartz in sinter deposits, which is an end member in the mineralogical transformation of the opal-A [25,44,64], allows us to infer intense dissolution and growth processes, which are not observed in steam-heated deposits, mainly constituted by opal-CT. This difference could suggest that the sinter deposits and their mineralogical transformation would have taken place prior to the formation of the steam-heated blanket.

Consequently, based on the silica phases recorded in the investigated alteration deposits, the following temporal sequence is proposed:

1. Precipitation of silicious sinters from alkaline spring discharges with microorganic activity, where the opal-A precipitation would have taken place. It currently appears as microcrystalline quartz in pinnacle-like silica deposits and silica deposits with coarse stratification.

2. Early dissolution/growth and transformation processes. During these processes, the transformation from opal-A to microcrystalline quartz begins, and the coexistence of characteristic morphologies such as nano-microstructures and hexagonal microcrystals (Figure 12) emphasize a gradual and gradational process. The transformation rates vary among sinters because post-depositional conditions can accelerate or delay these processes. Although reports regarding the transformation rates of opal to quartz are in the order of thousands of years [26], the different step of degree of crystallinity of the silica deposits cannot be directly extrapolated as time indicators because this process also depends on factors such as altitude, temperature, pH and sulfur deposits [26].

3. Alteration/precipitation in a steam-heated environment. At this period, the opal-CT in the silicified layer and the spread opal-CT with kaolinite-alunite-anatase in the friable layer would have formed and partially developed on sinter deposits.

4. Dissolution/growth and transformation processes are accelerated by acidic fluids. The development of transformation processes in the steam-heated environment would have been enhanced by bringing to the transformation of opal-CT to opal-C to quartz, with a predominance of this last phase, but coexisting with the preceding phases, thus suggesting a gradual transformation. Different authors recognize that the replacement of silica occurs laterally in the form of patch textures on a millimetric scale [25,26,44,69]. Putnis [70] reported that a change from one silica polymorph to another, such as from tridymite to cristobalite or quartz, requires bond breakage and the creation of a new structure. This process leads to reconstructive transformations and provides a mechanism for extremely fine-scale intergrowths between the different polymorphs, allowing the co-existence of more than one silica phase at any given time. It is possible that the presence of acidic fluids accelerated the transformation processes in the sinter deposits. Experimental studies [26] show that condensed acid vapors favor the transformation rate, dissolving opal-A and generating quartz after 21 weeks. Both in steam-heated blanket and sinters (to a lesser extent), dissolution textures show interaction with acidic fluids (Figure 12C).

5. Re-precipitation process associated with the present-day diffuse degassing fluxes. This actual event would be associated with dissolution and scarce and local formation of amorphous silica coupled with its transformation to opal-A, from acidic fluids. These variations in size and morphologies of the silica phases generate changes in the physical characteristics of the sinters. In general, there is an increase in density and a decrease in porosity with the development of mineralogical processes, although this tendency is still debated [44,71].

The sum of the data listed above makes it possible to differentiate the silica deposits associated with steam-heated blanket from previous relicts of siliceous sinter deposits. For the investigated deposits in the alteration zone of the CIVC, it is proposed that both the steam-heated blanket and the siliceous sinter deposits would be associated at depth with an active alkaline-chlorine geothermal environment. This is consistent with the high soil temperatures and the CO_2 diffuse degassing recorded by Taussi et al. [28]. In addition, neutral-pH water conditions were found in drilling cores for the clay cap of the Cerro Pabellón geothermal system [11] as well as for the propylitic zone, where pyrite and chalcopyrite with high metals concentrations were determined and associated with IS epithermal deposits [72,73].

5.3. Hydrothermal, Structural and Paleoclimatic Interactions in the Geothermal Systems of Northern Chile

Concerning the alteration zone of the CIVC, the interaction of the hydrothermal system, the structural setting and the paleo-climatic fluctuations all contributed, most likely, to the formation and evolution of the geothermal system. The role of these factors seems to be of major relevance in prospecting possible geothermal systems in other areas of northern Chile. As presented in this paper, the silica deposits of the CIVC are linked to a complex magmatic and hydrothermal history coupled with structural, paleoclimatic factors and sedimentary and mineralogical transformation processes, the results of which are recorded in the physical, chemical and biological changes of the alteration/precipitation of the investigated deposits.

The alteration zone of the CIVC was developed between 4800 m and 5200 m a.s.l. in the Atacama Desert, with little or no vegetation, low rainfall and surface runoff, which favor the excellent preservation conditions of processes and features associated with superficial and paleo-superficial landforms and the products of the hydrothermal system. Silica deposits located in the CIWS and the CIES associated with sinter deposits are characterized by biological remnants of diatoms and filaments that indicate surface freshwater bodies (not existing nowadays, Figure 15). This feature at 5100 m a.s.l. in the Atacama Desert, where water bodies are currently restricted to the presence of salt flats located at ~4000 m a.s.l., could be related to the last glaciation–deglaciation event that occurred

~20–10 ka ago [74–76]. The formation of fresh-water bodies could have therefore been associated with the availability of meltwater, constituting an appropriate environment for biological activity [75]. Furthermore, this contribution of meltwater to the substrate could have been a key factor in the fluid recharge for both the Cordón de Inacaliri and Cerro Pabellón geothermal reservoirs, giving rise to siliceous sinter deposits. In this sense, water samples from the Cerro Pabellón geothermal plant production wells indicate residence time within the order of several thousand years [77], comparable to the older paleo-sinter deposits of El Tatio, dated by ^{14}C [78] at 10.8 ka. As suggested by Morata et al. [77], these data support a long-lived fluid circulation and continuous geothermal activity, probably triggered by deglaciation in the Altiplano (~20–10 ka) [75]. Moreover, the distribution of sinter deposits shows a close spatial relation with the framework of fractures and/or lineaments array of the Pabelloncito graben. Recently, Taussi et al. [79] and [28] showed how diffuse soil CO_2 degassing circulation and soil temperature anomalies are controlled by NW- and ENE-striking lineaments of the graben, which are also a key factor in the mineralogical alteration/precipitation processes [12]; this work, Figure 15. In the CIVC, the higher CO_2 fluxes (>100 g m^{-2} d^{-1}) and temperatures (>55 °C) are not strictly related to the NW- or ENE-striking lineaments, but mainly occur at the intersection of both, suggesting that these two tectono-morphological lineaments play a fundamental role in controlling the ascent of the hydrothermal fluids [28], similarly to the Tolhuaca hydrothermal system [80].

Nevertheless, little is known about the fluctuation of the groundwater table during the Holocene, and consequently about the distance between the paleo-surfaces and paleo-groundwater tables in the Atacama Desert. Based on present-day records, it is assumed that this distance would have been variable, from zero close to low relief areas, up to several hundred meters in steep terrain, especially where arid climatic conditions prevail [81]. In addition, fluctuations at depth of the groundwater table would have taken place, which are associated with variations in the surface water discharge regime (neutral to alkaline-acidic) that are common in these types of high reliefs geothermal systems [44,82,83].

The aforementioned deglaciation process could have contributed to the formation of superficial aquifers that were heated by the remaining heat of volcanism in the graben (i.e., the youngest dacite domes erupted <150 ka [84]), giving rise to the formation of the steam-heated blanket. These acidic discharge fluids would have generated the immature silica deposits (opal-A, opal-A/CT) and dissolution/re-precipitation, associated with kaolinite-alunite-anatase, superimposed to the older sinter deposits.

The condensed acid vapor fluids from boiling processes generated in the deep geothermal reservoir, besides generating the steam-heated blanket, would have affected previous siliceous sinter deposits. These acid vapors would have been constituted by SO_4 and/or H_2S, which is inferred from the presence of alunite and gypsum and would have been responsible for accelerating the dissolution-precipitation processes.

Currently, a low rate of superficial fluids, consisting of steam and diffuse CO_2 with very little sulfur presence, dominates. This could be partially related with the low recharge rate of the system, mostly associated with the recharge of water produced during the last deglaciation. In addition, the descent in the groundwater table associated with fluctuations in the hydric water system of the region (which is consistent with the high-flow rate of geothermal fluids in the Tatio Geysers at 4200 m. a.s.l. [85] and 45 km far away from Cordón de Inacaliri) should be also considered. Another alternative hypothesis would be a decrease in enthalpy in this sector associated with the greater distance from the last dacite volcanism events located between Pampa Apacheta and the Apacheta-Aguilucho Volcanic Complex (Figure 1), close to the Cerro Pabellón geothermal plant [84,86].

In summary, the inter-relations between the structural setting of the Pabelloncito graben, the remnant of heat from the youngest dacitic volcanism in the area and the glaciation–deglaciation history in this region may have all contributed to the formation of the geothermal reservoirs in the Pabelloncito graben (i.e., Cerro Pabellón and Cordón Inacaliri areas) and would also be responsible for the hydrothermally altered volcanic rocks on the surface.

6. Conclusions

Six different mineral assemblages were identified in the surficial hydrothermal alteration zone (with distinct five domains) of the Cordón de Inacaliri volcanic complex (CIVC), allowing the definition of an acid-sulfate stage associated with the development of a geothermal system. The assemblages (i) kaolinite + alunite + opal-CT + anatase; (ii) alunite + gypsum; and (v) opal-CT all define an acid-sulfate alteration, whereas (iv) kaolinite + hematite + halloysite + smectite + I/S + illite represents an argillic alteration. The mineral assemblages of the acid-sulfate alteration match well with a steam-heated environment associated laterally with clay phases such as smectites or mixed layer I/S. On the other hand, the mineral assemblages (vi) microcrystalline quartz, together with remnants of microorganisms (*Thalassionema nitzschioides (Grunow) Mereschkowsky*, *Cocconeis Placentula Ehrenberg*, *Amphora* sp. diatoms and remnants of filaments) in microcrystalline quartz deposits, define sinter deposits linked to alkaline-chlorine water hot springs laterally associated with (iii) calcite + aragonite deriving from bicarbonate waters. The analyzed surface data cluster allows us to link the paleosurface products with a still active, recently discovered, geothermal system at depth with an estimated preliminary potential of ~1.08 MWe·km^{-2} [28].

Detailed silica phase studies within the alteration zone of the CIVC show five clearly differentiated steps of mineralogical transformation corresponding to the opal–quartz sequence and peculiar features for the deposits associated with two different discharge fluid. As part of the deposits associated with the steam-heated blanket, we identified that the first three phases are marked by the prevalence of opal-A, opal-A/CT and opal-CT, which appear as massive silica accumulated in mud pots, and spread opal-CT within the kaolinite + alunite + opal-CT + anatase assemblage, indicating discharge products associated with acid fluids. In the sinter deposits, typical of alkali-chloride hot spring discharges, we identified: 1- discontinuous pinnacle-like silica deposits and 2- silica deposits with laterally developed coarse stratification. Paracrystalline to microcrystalline phases such as opal-C and quartz prevail in both deposits. Here, the presence of diatoms and microbe filaments indicate alkaline/freshwater/brackish water bodies. The scarce presence of relics of sinter deposits, with a high degree of crystallinity phases and diatoms remnants, in addition to sulfate deposits, are consistent with the overlapping of a steam-heated environment to a previous sinter environment. The coexistence and association of steam-heated blanket with sinters deposits is peculiar of geothermal systems, and similar to what was found at Cerro Pabellón, which could host an IS epithermal environment.

The areal distribution of the steam-heated blanket shows a close relationship with the structural configuration of the graben, with a greater development along the NW lineaments parallel to the main structure and at the intersection zones with ENE lineaments, in agreement with the spatial arrangement of the soil CO_2 flux and temperature anomalies [28]. The presence of diatoms and microorganisms at 5100 m a.s.l. in the Atacama Desert associated with heated freshwater bodies could also have had a relationship with the last documented deglaciation in the area (~20–10 ka) [75] that could have been represented an important factor in the recharge of the geothermal systems within the graben.

In the case of the mineralogical alteration zone of the CIVC, the interaction of the hydrothermal system, the structural setting, the recent acid (dacite) magmatic activity and the paleo-climatic fluctuations closely match in the generation and evolution of the geothermal system, allowing the development of an acid-sulfate stage, which was recorded at the surface by early sinters with remnants of microorganisms and later with the overlay of a steam-heated blanket.

As pointed out for the Cordón de Inacaliri (1.08 MWe·km^{-2}) and Cerro Pabellón (48 + 33 MWe) geothermal systems, both representing hidden reservoirs within the Pabelloncito graben, the present study unravels key factors and processes which are of paramount importance in the exploration of other hidden geothermal systems throughout the Altiplano Puna of the Central Andes.

References

1. Aravena, D.; Muñoz, M.; Morata, D.; Lahsen, A.; Parada, M.A.; Dobson, P. Assessment of high enthalpy geothermal resources and promising areas of Chile. *Geothermics* **2016**, *59*, 1–13. [CrossRef]
2. Mesa de Geotermia. *Rol de la Geotermia en el Desarrollo de la Matriz Eléctrica Chilena*; Ministerio de Energía: Santiago, Chile, 2018; Volume 66. Available online: http://www.minenergia.cl/mesa-geotermia (accessed on 3 July 2018).
3. Sillitoe, R.H. Epithermal paleosurfaces. *Miner. Deposita* **2015**, *50*, 767–793. [CrossRef]
4. Chang, Z.; Hedenquist, J.; White, N.C.; Cooke, D.; Roach, M.; Deyell, C.L.; Garcia, J.; Gemmell, J.B.; McKnight, S.; Cuison, A.L. Exploration Tools for Linked Porphyry and Epithermal Deposits: Example from the Mankayan Intrusion-Centered Cu-Au District, Luzon, Philippines. *Econ. Geol.* **2011**, *106*, 1365–1398. [CrossRef]
5. Bobos, I.; Gomes, C. Mineralogy and Geochemistry (HFSE and REE) of the Present-Day Acid-Sulfate Types Alteration from the Active Hydrothermal System of Furnas Volcano São Miguel Island, The Azores Archipelago. *Minerals* **2021**, *11*, 355. [CrossRef]
6. Sepúlveda, F.; Lahsen, A. Geothermal exploration in central southern Chile (33°–4°2S). *Geotherm. Resour. Council Trans.* **2003**, *27*, 635–638.
7. Sepúlveda, F.; Lahsen, A.; Dorsch, K.; Palacios, C.; Bender, S. Geothermal Exploration in the Cordón Caulle Region, Southern Chile. In Proceedings of the World Geothermal Congress, Antalya, Turkey, 24–29 April 2005; pp. 24–29.
8. Procesi, M. Geothermal Potential Evaluation for Northern Chile and Suggestions for New Energy Plans. *Energies* **2014**, *7*, 5444–5459. [CrossRef]
9. Urzua, L.; Powell, T.; Cumming, W.B.; Dobson, P. Apacheta, a new geothermal prospect in northern Chile. *Geotherm. Resour. Counc.* **2002**, *26*, 65–69.
10. Tassi, F.; Aguilera, F.; Darrah, T.; Vaselli, O.; Capaccioni, B.; Poreda, R.; Huertas, A.D. Fluid geochemistry of hydrothermal systems in the Arica-Parinacota, Tarapacá and Antofagasta regions (northern Chile). *J. Volcanol. Geotherm. Res.* **2010**, *192*, 1–15. [CrossRef]
11. Maza, S.N.; Collo, G.; Morata, D.; Lizana, C.; Camus, E.; Taussi, M.; Renzulli, A.; Mattioli, M.; Godoy, B.; Alvear, B.; et al. Clay mineral associations in the clay cap from the Cerro Pabellón blind geothermal system, Andean Cordillera, Northern Chile. *Clay Miner.* **2018**, *53*, 117–141. [CrossRef]
12. Maza, S.N.; Collo, G.; Morata, D.; Taussi, M.; Vidal, J.; Mattioli, M.; Renzulli, A. Active and fossil hydrothermal zones of the Apacheta volcano: Insights for the Cerro Pabellón hidden geothermal system (Northern Chile). *Geothermics* **2021**, *96*, 102206. [CrossRef]
13. Inostroza, M.; Aguilera, F.; Menzies, A.; Layana, S.; González, C.; Ureta, G.; Sepúlveda, J.; Scheller, S.; Böehm, S.; Barraza, M.; et al. Deposition of metals and metalloids in the fumarolic fields of Guallatiri and Lastarria volcanoes, northern Chile. *J. Volcanol. Geotherm. Res.* **2020**, *393*, 106803. [CrossRef]
14. Munoz-Saez, C.; Manga, M.; Hurwitz, S. Hydrothermal discharge from the El Tatio basin, Atacama, Chile. *J. Volcanol. Geotherm. Res.* **2018**, *361*, 25–35. [CrossRef]
15. Hedenquist, J.W.; Arribas, A., Jr.; Gonzales-Urien, E. Exploration for epithermal gold deposits. *Rev. Econ. Geol.* **2000**, *13*, 245–277.
16. Hedenquist, J.; Taran, Y.A. Modeling the Formation of Advanced Argillic Lithocaps: Volcanic Vapor Condensation Above Porphyry Intrusions. *Econ. Geol.* **2013**, *108*, 1523–1540. [CrossRef]
17. Hedenquist, J.; Arribas, A. Exploration Implications of Multiple Formation Environments of Advanced Argillic Minerals. *Econ. Geol.* **2021**, 35. [CrossRef]

18. Bignall, G.; Browne, P. Surface hydrothermal alteration and evolution of the Te Kopia Thermal Area, New Zealand. *Geothermics* **1994**, *23*, 645–658. [CrossRef]

19. Cumming, W. Geothermal resource conceptual models using surface exploration data. In Proceedings of the Thirty-Fourth Workshop on Geothermal Reservoir Engineering, Stanford, CA, USA, 9–11 February 2009.

20. Longo, A.A.; Dilles, J.H.; Grunder, A.L.; Duncan, R. Evolution of Calc-Alkaline Volcanism and Associated Hydrothermal Gold Deposits at Yanacocha, Peru. *Econ. Geol.* **2010**, *105*, 1191–1241. [CrossRef]

21. Chang, Z.; Hedenquist, J.W.; White, N.C.; Cooke, D.R.; Deyell, C.L.; Garcia, J. New tools for exploring lithocaps: Example from the Mankayan intrusion-centered Cu-Au district, Philippines. In *Smart Science for Exploration and Mining, Proceedings of the Tenth Biennial SGA Meeting, Townsville, Australia, 17–20 August 2009*; James Cook University School of Earth & Environmental Studies, Economic Geology Research Unit: Townsville, Australia, 2009; Volume 2, pp. 707–709.

22. Jourdan, A.-L.V.; Mullis, J.; Ramseyer, K.; Spiers, C. Evidence of growth and sector zoning in hydrothermal quartz from Alpine veins. *Eur. J. Miner.* **2009**, *21*, 219–231. [CrossRef]

23. Fournier, R.O.; Rowe, J.J. Estimation of underground temperatures from the silica content of water from hot springs and wet-steam wells. *Am. J. Sci.* **1966**, *264*, 685–697. [CrossRef]

24. Fournier, R.O. The Behaviour of Silica in Hydrothermal Solutions. *Rev. Econ. Geol.* **1985**, *2*, 45–62.

25. Lynne, B.Y.; Campbell, K.A.; Moore, J.N.; Browne, P.R.L. Diagenesis of 1900-year-old siliceous sinter (opal-A to quartz) at Opal Mound, Roosevelt Hot Springs, Utah, U.S.A. *Sediment. Geol.* **2005**, *179*, 249–278. [CrossRef]

26. Lynne, B.Y.; Campbell, K.A.; Perry, R.S.; Browne, P.; Moore, J. Acceleration of sinter diagenesis in an active fumarole, Taupo volcanic zone, New Zealand. *Geology* **2006**, *34*, 749. [CrossRef]

27. Lynne, B.Y. Siliceous sinter: An early exploration tool and direct link to a geothermal reservoir. In Proceedings of the Thirty-Eighth Workshop on Geothermal Reservoir Engineering Stanford University, Stanford, CA, USA, 11–13 February 2013; pp. 11–13.

28. Taussi, M.; Nisi, B.; Vaselli, O.; Maza, S.; Morata, D.; Renzulli, A. Soil CO2 flux and temperature from a new geothermal area in the Cordón de Inacaliri Volcanic Complex (northern Chile). *Geothermics* **2021**, *89*, 101961. [CrossRef]

29. Francis, P.W.; Rundle, C.C. Rates of production of the main magma types in the central Andes. *GSA Bull.* **1976**, *87*, 474. [CrossRef]

30. Wörner, G.; Hammerschmidt, K.; Henjes-Kunst, F.; Lezaun, J.; Wilke, H. Geochronology (40Ar/39Ar, K-Ar and He-exposure ages) of Cenozoic magmatic rocks from northern Chile (18–22°S): Implications for magmatism and tectonic evolution of the central Andes. *Rev. Geol. Chile* **2000**, *27*, 205–240.

31. Sellés, D.; Gardeweg, M. Geología del área Ascotán-Cerro Inacaliri, Región de Antofagasta. In *Servicio Nacional de Geología y Minería, Carta Geológica de Chile*; Serie Geología Básica No. 190 73; SERNAGEOMIN: Santiago, Chile, 2017. [CrossRef]

32. Tibaldi, A.; Bonali, F. Contemporary recent extension and compression in the central Andes. *J. Struct. Geol.* **2018**, *107*, 73–92. [CrossRef]

33. Tibaldi, A.; Rust, D.; Corazzato, C.; Merri, A. Setting the scene for self-destruction: From sheet intrusions to the structural evolution of rifted stratovolcanoes. *Geosphere* **2010**, *6*, 189–210. [CrossRef]

34. Veloso, E.E.; Tardani, D.; Elizalde, D.; Godoy, B.; Sánchez-Alfaro, P.A.; Aron, F.; Reich, M.; Morata, D. A review of the geo-dynamic constraints on the development and evolution of geothermal systems in the Central Andean Volcanic Zone (18–28°Lat.S). *Inter. Geol. Rev.* **2019**, *61*, 1–25.

35. Putz, H.; Brandenburg, K. *Match!—Phase Analysis Using Powder Diffraction, Version 3.x*; Crystal Impact—GbR: Bonn, Germany, 2021; Available online: https://www.crystalimpact.de/match (accessed on 3 March 2021).

36. Hubbard, C.R.; Snyder, R.L. RIR—Measurement and Use in Quantitative XRD. *Powder Diffr.* **1988**, *3*, 74–77. [CrossRef]

37. Jones, J.B.; Segnit, E.R. The nature of opal I. nomenclature and constituent phases. *J. Geol. Soc. Aust.* **1971**, *18*, 57–68. [CrossRef]

38. Flörke, O.W.; Graetsch, H.; Martin, B.; Röller, K.; Wirth, R. Nomenclature of micro-and non-crystalline silica minerals, based on structure and microstructure. *Neues Jahrbuch Mineralogie. Abhandlungen* **1991**, *163*, 19–42.

39. Graetsch, H. Structural characteristics of opaline and microcrystalline silica minerals. *Silica* **1994**, *29*, 209–232. [CrossRef]

40. Lynne, B.Y.; Campbell, K.A. Diagenetic transformations (opal-A to quartz) of low- and mid-temperature microbial textures in siliceous hot-spring deposits, Taupo Volcanic Zone, New Zealand. *Can. J. Earth Sci.* **2003**, *40*, 1679–1696. [CrossRef]

41. Lynne, B.Y.; Campbell, K. Morphologic and Mineralogic Transitions from Opal-A to Opal-CT in Low-Temperature Siliceous Sinter Diagenesis, Taupo Volcanic Zone, New Zealand. *J. Sediment. Res.* **2004**, *74*, 561–579. [CrossRef]

42. Jones, B.; Renaut, R.W. Microstructural changes accompanying the opal-A to opal-CT transition: New evidence from the siliceous sinters of Geysir, Haukadalur, Iceland. *Sedimentology* **2007**, *54*, 921–948. [CrossRef]

43. Herdianita, N.; Rodgers, K.A.; Browne, P.R. Routine instrumental procedures to characterise the mineralogy of modern and ancient silica sinters. *Geothermics* **2000**, *29*, 65–81. [CrossRef]

44. Lynne, B.Y.; Campbell, K.; Moore, J.; Browne, P. Origin and evolution of the Steamboat Springs siliceous sinter deposit, Nevada, U.S.A. *Sediment. Geol.* **2008**, *210*, 111–131. [CrossRef]

45. Moore, D.M.; Reynolds, R.C., Jr. *X-ray Diffraction and the Identification and Analysis of Clay Minerals*; Oxford University Press: Oxford, UK, 1997; p. 378.

46. Aparicio, P.; Galán, E.; Ferrell, R.E. A new kaolinite order index based on XRD profile fitting. *Clay Miner.* **2006**, *41*, 811–817. [CrossRef]

47. Sbrana, A.; Fulignati, P.; Marianelli, P.; Boyce, A.; Cecchetti, A. Exhumation of an active magmatic–hydrothermal system in a resurgent caldera environment: The example of Ischia (Italy). *J. Geol. Soc.* **2009**, *166*, 1061–1073. [CrossRef]

48. Zimbelman, D.R.; Rye, R.O.; Breit, G.N. Origin of secondary sulfate minerals on active andesitic stratovolcanoes. *Chem. Geol.* **2005**, *215*, 37–60. [CrossRef]

49. Africano, F.; Bernard, A. Acid alteration in the fumarolic environment of Usu volcano, Hokkaido, Japan. *J. Volcanol. Geotherm. Res.* **2000**, *97*, 475–495. [CrossRef]

50. Adams, P.M.; Lynch, D.K.; Buckland, K.N.; Johnson, P.D.; Tratt, D.M. Sulfate mineralogy of fumaroles in the Salton Sea Geothermal Field, Imperial County, California. *J. Volcanol. Geotherm. Res.* **2017**, *347*, 15–43. [CrossRef]

51. Piochi, M.; Mormone, A.; Balassone, G. Hydrothermal alteration environments and recent dynamics of the Ischia volcanic island (southern Italy): Insights from repeated field, mineralogical and geochemical surveys before and after the 2017 Casamicciola earthquake. *J. Volcanol. Geotherm. Res.* **2019**, *376*, 104–124. [CrossRef]

52. Ercan, H.Ü.; Ece, Ö.I.; Schroeder, P.A.; Karacik, Z. Differentiating Styles of Alteration Within Kaolin-Alunite Hydrothermal Deposits of Çanakkale, NW Turkey. *Clays Clay Miner.* **2016**, *64*, 245–274. [CrossRef]

53. Dill, H.G. Kaolin: Soil, rock and ore: From the mineral to the magmatic, sedimentary and metamorphic environments. *Earth Sci. Rev.* **2016**, *161*, 16–129. [CrossRef]

54. Sillitoe, R.H.; Hedenquist, J.W. Linkages between volcanotectonic settings, ore fluid compositions and epithermal precious metal deposits. In *Volcanic, Geothermal and Ore-forming Fluids: Rulers and Witnesses of Processes within the Earth*; Simmons, S.F., Graham, I., Eds.; Society of Economic Geologists (SEG): Littleton, CO, USA, 2003; Volume 10, pp. 315–343.

55. Pirajno, F. *Hydrothermal Processes and Mineral Systems*; Springer Science & Business Media: Berlin, Germany, 2008.

56. Sillitoe, R.H. Porphyry Copper Systems. *Econ. Geol.* **2010**, *105*, 3–41. [CrossRef]

57. Hedenquist, J.; Browne, P.R. The evolution of the Waiotapu geothermal system, New Zealand, based on the chemical and isotopic composition of its fluids, minerals and rocks. *Geochim. Cosmochim. Acta* **1989**, *53*, 2235–2257. [CrossRef]

58. Hedenquist, J.W. Boiling and dilution in the shallow portion of the Waiotapu gethermal system, New Zealand. *Geochim. Cosmochim. Acta.* **1991**, *55*, 2753–2765. [CrossRef]

59. Inoue, A. Formation of clay minerals in hydrothermal environments. In *Origin and Mineralogy of Clays*; Velde, B., Ed.; Springer: Berlin, Germany, 1995; pp. 268–329.

60. Simmons, S.F.; Browne, P.R.L.; Arehart, G.B.; Hulston, J.R. Illite, illite-smectite and smectite occurrences in the Broad-lands-Ohaaki geothermal system and their implications for clay mineral geothermometry. *Water Rock Interact.* **1998**, *9*, 691–694.

61. Patrier, P.; Beaufort, D.; Mas, A.; Traineau, H. Surficial clay assemblage associated with the hydrothermal activity of Bouillante (Guadeloupe, French West Indies). *J. Volcanol. Geotherm. Res.* **2003**, *126*, 143–156. [CrossRef]

62. Stimac, J.; Goff, F.; Goff, C.J. Intrusion-Related Geothermal Systems. In *The Encyclopedia of Volcanoes*, 2nd ed.; Sigurdsson, H., Ed.; Academic Press: Amsterdam, The Netherlands, 2015; pp. 799–822. [CrossRef]

63. White, N.C.; Hedenquist, J.W. Epithermal Gold Deposits: Styles, characteristics and exploration. *SEG Discov.* **1995**, *1*, 1–13. [CrossRef]

64. Lynne, B.Y.; Campbell, K.; James, B.; Browne, P.R.L.; Moore, J. Tracking crystallinity in siliceous hot-spring deposits. *Am. J. Sci.* **2007**, *307*, 612–641. [CrossRef]

65. Lynne, B.Y. Impact of three common post-depositional environmental settings on siliceous sinter diagenesis: An eight year experiment. *J. Volcanol. Geotherm. Res.* **2015**, *292*, 84–101. [CrossRef]

66. White, D.; Thompson, G.; Sandberg, C. Rocks, structure, and geologic history of Steamboat Springs thermal area, Washoe County, Nevada. *Geolog. Sur. Prof. Pap.* **1964**, *458-B*, 1–63.

67. Cady, S.L.; Farmer, J.D. Fossilization Processes in Siliceous Thermal Springs: Trends in Preservation Along Thermal Gradients. In *Evolution of Hydrothermal Ecosystems on Earth (and Mars?), Proceedings of the CIBA Foundation Symposium, London, UK, 30 January–1 February 1996*; Bock, G.R., Goode, J.A., Eds.; Wiley: Chichester, UK, 1996; Volume 202, pp. 150–173.

68. Ritter, B.; Wennrich, V.; Medialdea, A.; Brill, D.; King, G.; Schneiderwind, S.; Niemann, K.; Fernández-Galego, E.; Diederich, J.; Rolf, C.; et al. Climatic fluctuations in the hyperarid core of the Atacama Desert during the past 215 ka. *Sci. Rep.* **2019**, *9*, 1–13. [CrossRef]

69. Campbell, K.; Sannazzaro, K.; Rodgers, K.; Herdianita, N.; Browne, P. Sedimentary Facies and Mineralogy of the Late Pleistocene Umukuri Silica Sinter, Taupo Volcanic Zone, New Zealand. *J. Sediment. Res.* **2001**, *71*, 727–746. [CrossRef]

70. Putnis, A. *Introduction to Mineral Sciences*; Cambridge University Press: Cambridge, UK, 1992.

71. Herdianita, N.R.; Browne, P.R.L.; Rodgers, K.A.; Campbell, K.A. Mineralogical and textural changes accompanying ageing of silica sinter. *Miner. Deposita* **2000**, *35*, 48–62. [CrossRef]

72. Román, N.; Reich, M.; Leisen, M.; Morata, D.; Barra, F.; Deditius, A. Geochemical and micro-textural fingerprints of boiling in pyrite. *Geochim. Cosmochim. Acta* **2019**, *246*, 60–85. [CrossRef]

73. Reich, M.; Román, N.; Barra, F.; Morata, D. Silver-Rich Chalcopyrite from the Active Cerro Pabellón Geothermal System, Northern Chile. *Minerals* **2020**, *10*, 113. [CrossRef]

74. Ward, D.J.; Cesta, J.M.; Galewsky, J.; Sagredo, E. Late Pleistocene glaciations of the arid subtropical Andes and new results from the Chajnantor Plateau, northern Chile. *Quat. Sci. Rev.* **2015**, *128*, 98–116. [CrossRef]

75. Blard, P.-H.; Lave, J.; Farley, K.; Ramirez, V.; Jimenez, N.; Martin, L.; Charreau, J.; Tibari, B.; Fornari, M. Progressive glacial retreat in the Southern Altiplano (Uturuncu volcano, 22°S) between 65 and 14 ka constrained by cosmogenic 3He dating. *Quat. Res.* **2014**, *82*, 209–221. [CrossRef]

76. Godoy, B.; Rodríguez, I.; Pizarro, M.; Rivera, G. Geomorphology, lithofacies, and block characteristics to determine the origin, and mobility, of a debris avalanche deposit at Apacheta-Aguilucho Volcanic Complex (AAVC), northern Chile. *J. Volcanol. Geotherm. Res.* **2017**, *347*, 136–148. [CrossRef]

77. Morata, D.; Reich, M.; Muñoz-Saez, C.; Daniele, L.; Rivera, G.; Volpi, G.; Cecioni, M.; Guidetti, G.; Cappetti, G. Origin and age of fluids at the Cerro Pabellón Geothermal System, Northern Chile. In Proceedings of the 41st New Zealand Geothermal Workshop, Auckland, New Zealand, 25–27 November 2019.

78. Slagter, S.; Reich, M.; Munoz-Saez, C.; Southon, J.; Morata, D.; Barra, F.; Gong, J.; Skok, J. Environmental controls on silica sinter formation revealed by radiocarbon dating. *Geology* **2019**, *47*, 330–334. [CrossRef]

79. Taussi, M.; Nisi, B.; Pizarro, M.; Morata, D.; Veloso, E.A.; Volpi, G.; Vaselli, O.; Renzulli, A. Sealing capacity of clay-cap units above the Cerro Pabellón hidden geothermal system (northern Chile) derived by soil CO_2 flux and temperature measurements. *J. Volcanol. Geotherm. Res.* **2019**, *384*, 1–14. [CrossRef]

80. Collignon, M.; Cardellini, C.; Duprat-Oualid, S.; Øyvind, H.; Chiodini, G.; Vandemeulebrouck, J.; Gonzalez-Vidal, D.; Espinoza, A.; Tassara, A.; Ruch, J. Carbon dioxide diffuse emission at the Tolhuaca hydrothermal system (Chile) controlled by tectonics and topography. *J. Volcanol. Geotherm. Res.* **2021**, *417*, 107316. [CrossRef]

81. Houston, J.; Hartley, A.J. The Central Andean west-slope rainshadow and its potential contribution to the origin of hyper-aridity in the Atacama desert. *Int. J. Climatol.* **2003**, *23*, 1453–1464. [CrossRef]

82. Houston, J. Variability of precipitation in the Atacama Desert: Its causes and hydrological impact. *Int. J. Climatol.* **2006**, *26*, 2181–2198. [CrossRef]

83. Rech, J.A.; Quade, J.; Betancourt, J.L. Late Quaternary paleohydrology of the central Atacama Desert (lat 22–24 S.), Chile. *Geolog. Soc. Amer. Bul.* **2002**, *114*, 334–348. [CrossRef]

84. Renzulli, A.; Menna, M.; Tibaldi, A.; Flude, S. New data of surface geology, petrology and Ar-Ar geochronology of the Alti-plano-Puna Volcanic Complex (northern Chile) in the framework of future geothermal exploration. In Proceedings of the XI Congreso Geólogico Chileno, Antofagasta, Chile, 7–11 August 2006.

85. Wilmeth, D.T.; Nabhan, S.; Myers, K.D.; Slagter, S.; Lalonde, S.V.; Sansjofre, P.; Homann, M.; Konhauser, K.O.; Munoz-Saez, C.; van Zuilen, M.A. Depositional evolution of an extinct sinter mound from source to outflow, El Tatio, Chile. *Sediment. Geol.* **2020**, *406*, 105726. [CrossRef]

86. Taussi, M.; Godoy, B.; Piscaglia, F.; Morata, D.; Agostini, S.; Le Roux, P.; González-Maurel, O.; Gallmeyer, G.; Menzies, A.; Renzulli, A. The upper crustal magma plumbing system of the Pleistocene Apacheta-Aguilucho Volcanic Complex area (Altiplano-Puna, northern Chile) as inferred from the erupted lavas and their enclaves. *J. Volcanol. Geotherm. Res.* **2019**, *373*, 179–198. [CrossRef]